JTSES
Journal of Thermal and Sustainable Energy Systems
https://jtses.com/index.php/home/index

AI-Enabled Wire-Arc Additive Manufacturing of TiB_2-Modified Recycled AA7075 for Crack-Resistant Aerospace Structure

Sankar Thangavel [1]*, Divya Ponnusamy [2], Kannan Thanneerpanthalpalayam Kandasamy [3], J. Mahendran [4]

[1] Department of Mechanical Engineering, Paavai College of Engineering, Namakkal – 637018, Tamil Nadu, India — Email: ersankar.t@gmail.com

[2] Department of Physics, Paavai Engineering College, Namakkal – 637018, Tamil Nadu, India — Email: dhivya6d3@yahoo.com

[3] Department of Mechanical Engineering, Jerusalem College of Engineering, Chennai, Tamil Nadu, India — Email: kannantkster@gmail.com

[4] Department of Mechanical Engineering, Kongunadu College of Engineering and Technology (KNCET), Tiruchirappalli, Tamil Nadu, India — Email: mahebalaji123@gmail.com

Corresponding Author*: Sankar Thangavel — Email: ersankar.t@gmail.com

ABSTRACT:

The high-strength AA7075 aluminum alloy is attractive for aerospace and defense structures because of its favorable strength-to-weight ratio; however, its susceptibility to solidification cracking restricts its processing through wire-arc additive manufacturing. Simultaneously, the growing quantity of high-grade aluminum machining waste creates a need for direct and value-added recycling. This study developed a crack-resistant recycled AA7075 feedstock modified with in-situ TiB_2 grain refiners for wire-arc additive manufacturing of lightweight strategic components. Clean AA7075 machining chips were remelted, compositionally corrected, and converted into welding wires containing controlled TiB_2 additions. Wall structures were deposited by varying the wire-feed rate, travel speed, current, interpass temperature, and TiB- concentration. High-speed thermal imaging, arc-voltage signals, and acoustic emission data were recorded during deposition. A physics-informed machine-learning framework combining thermal-history constraints with XGBoost and Gaussian-process regression was used to predict the porosity, hot crack density, grain size, and mechanical anisotropy. The deposited structures were examined using X-ray computed tomography, optical microscopy, scanning electron microscopy, electron backscatter diffraction, and X-ray diffraction. Tensile, hardness, fracture toughness, and fatigue tests is performed to determine the relationship between process stability, TiB--induced heterogeneous nucleation, and structural performance. The life-cycle energy consumption and material recovery were also compared with those of conventionally produced AA7075. The principal novelty is the integration of recycled aerospace-grade aluminum, nanoparticle-assisted grain refinement, multimodal in situ sensing, and physically constrained defect prediction in a single additive-manufacturing framework. This study is expected to establish a closed-loop route for transforming aluminum waste into qualified, geometrically complex components while reducing hot cracking, process uncertainty, and dependence on primary aluminum.

Keywords: Recycled AA7075; wire-arc additive manufacturing; titanium diboride; hot cracking; physics-informed learningisIntroduction

INTRODUCTION

High-strength aluminum alloys were widely considered for aerospace and defense structures because substantial mass savings were enabled by their high specific strength, established heat-treatment response, and mature engineering use. Among available large-scale metal additive-manufacturing routes, wire-arc additive manufacturing (WAAM) was increasingly examined because high deposition rates, comparatively low equipment costs, and efficient wire utilization were provided. Nevertheless, aluminum WAAM remained constrained by repeated thermal cycling, hydrogen-related porosity, oxide entrainment, residual stress, geometric instability, and crystallographic anisotropy. These limitations were shown to depend jointly on alloy chemistry, solidification behavior, arc mode, heat input, shielding, and interpass thermal management rather than on any single process variable (Langelandsvik et al., 2021). A similar dependence was identified across broader aluminum arc-additive-

manufacturing studies, in which defect control and mechanical performance were strongly affected by coupled process and post-process conditions (Sinha et al., 2022). Particular concern was associated with 7xxx-series alloys because their broad freezing ranges and compositionally sensitive terminal liquid films promoted solidification cracking, while Zn and Mg volatilization complicated compositional stability. Consequently, additional research on 7xxx alloys, environmental sustainability, and defect mitigation was identified as necessary in recent aluminum-WAAM assessments (Sarıkaya et al., 2024). Lower-energy CMT variants were associated with controllable layer geometry, temperature histories, and porosity in AlMg5Mn deposits (Gierth et al., 2020). Response-surface optimization of double-pulsed GMAW further demonstrated that deposition geometry and microstructure were strongly governed by coupled arc and travel parameters (Du et al., 2023). In CMT-WAAM AA2319, local porosity, heterogeneous grain bands, and brittle second phases were subsequently associated with orientation-dependent deformation and fracture behavior (Pan et al., 2024). ()

The thermal origin of these responses was further resolved through numerical, optical, and signal-based investigations. Deposition geometry and aluminum-alloy microstructure evolution were reproduced through coupled finite-element and phase-field modelling, through which process parameters were connected to temperature gradients and dendritic development (Geng et al., 2021). High-speed imaging of aluminum WAAM showed that unstable track formation was associated with both torch orientation and interlayer-temperature conditions, thereby demonstrating that nominal machine settings alone were insufficient for stability assessment (Hauser et al., 2020). Oxidation anomalies were also resolved through high-speed observation, computational fluid dynamics, and optical-emission analysis, which linked surface-oxide formation to the local deposition environment (Hauser et al., 2021a). Because the interpass temperature was governed by accumulated heat and idle time, finite-element simulations coupled with artificial neural networks were used to generate thermal process maps for multilayer WAAM walls (Farias et al., 2021). These findings established a direct requirement for synchronized thermal, electrical, geometric, and acoustic observations when spatially localized defects were to be attributed to their actual process histories. studies that addressed material modification, porosity control, sensing, learning, and recycling were compared in Table 1. ()

Table 1. studies relevant to particle-modified aluminum WAAM, defect control, process monitoring, data-driven prediction, and aluminum recycling.

Reference/Citation	Objective/Aim	Methodology/Approach	Materials/Parameters Studied	Key Findings/Results	Relevance to Current Study
Shen et al. (2023a) ()	Process TiB_2-reinforced AA7075 by variable-polarity arc deposition	Variable-polarity TIG; microscopy; tensile testing	AA7075 wire; TiB_2 nanoparticles; build position	△ Crack-free deposition with refined grains and stronger tensile response	Direct precedent for TiB_2-modified 7xxx arc additive manufacturing
Shen et al. (2023b) ()	Evaluate heat treatment of TiB_2-modified AA7075 deposits	T6 treatment; microscopy; tensile and corrosion testing	TiB_2/AA7075; solution treatment; artificial aging	△ T6 treatment strengthened deposits and homogenized second-phase distribution	Defined precipitation-control requirements after deposition

Reference/Citation	Objective/Aim	Methodology/Approach	Materials/Parameters Studied	Key Findings/Results	Relevance to Current Study
Li et al. (2025) ()	Compare TiB_2 and TiC crack-control mechanisms	WAAM; heat treatment; microscopy; fatigue testing	Al–Mg–Si; TiB_2; TiC particles	△ Particle modification suppressed hot cracking through fine equiaxed solidification	Supported particle-dispersion and fatigue assessment
Yang et al. (2022) ()	Characterize TiB_2 aluminum-composite CMT-WAAM	CMT deposition; T6 treatment; microscopy; tensile testing	TiB_2/AlSi7Mg0.6; build orientation	△ TiB_2 refinement weakened anisotropy after CMT deposition and T6 treatment	Informed grain refinement and orientation analysis
Arana et al. (2021) ()	Control porosity in aluminum WAAM	CMT; shielding variation; alternative deposition strategies	Al–Mg wire; gas flow; trajectory	▽ Controlled shielding and deposition strategy lowered aluminum WAAM porosity	Established shielding and hydrogen-control considerations
Hauser et al. (2021b) ()	Resolve porosity formation and monitoring routes	WAAM; imaging; CFD; porosity characterization	AlSi5; shielding-gas flow; surface cavities	▽ Lower gas flow prolonged melt-pool life and limited porosity	Linked process sensing with pore formation
Baier et al. (2023) ()	Establish quantitative WAAM thermal monitoring	Thermography; emissivity calibration; thermocouple validation	Interlayer temperature; emissivity; transmittance	△ Calibrated thermography enabled absolute interlayer-temperature monitoring	Supported traceable thermal-history measurement
Xiao et al. (2022) ()	Predict WAAM geometry and select process parameters	Machine learning; multivariate geometry modelling; inverse selection	Wire feed; travel speed; bead geometry	△ Machine learning predicted geometry and supported inverse parameter selection	Supported data-driven process–geometry modelling

Reference/Citation	Objective/Aim	Methodology/Approach	Materials/Parameters Studied	Key Findings/Results	Relevance to Current Study
Zhang et al. (2024) ()	Identify DED-arc defects from acoustic signals	Wavelet transformation; CNN classification; acoustic monitoring	Acoustic signatures; discontinuities; pores	△ Acoustic wavelet-CNN models classified DED-arc defects with high accuracy	Supported multimodal in situ defect detection
El Mehtedi et al. (2023) ()	Compare environmental performance of aluminum-chip recycling	Life-cycle assessment; direct rolling; accumulative roll bonding	Aluminum chips; energy; environmental impacts	▽ Solid-state recycling produced lower environmental burdens than remelting routes	Established recycling and environmental-accounting context

Machine-learning research was subsequently broadened from isolated bead-property regressions toward process monitoring, transferability, and physically constrained prediction. Across WAAM studies, machine learning was applied to design, defect detection, process optimization, and materials characterization, although restricted datasets and limited model transferability remained persistent concerns (Hamrani et al., 2024). Surface roughness was predicted from WAAM conditions using ANFIS, extreme-learning-machine, and support-vector-regression approaches, but the resulting models remained tied to the experimental parameter space from which training data had been generated (Xia et al., 2022). Automated bead modelling was also constructed through industrial information integration and support-vector-machine learning, by which parameter combinations were selected from bead-geometry targets (Ding et al., 2021). Transfer of predicted temperature histories across aluminum WAAM geometries was examined using multilayer perceptrons, and prediction error was shown to depend on the degree and type of extrapolation from the training condition (Fagersand et al., 2024). More broadly, physics-informed learning was proposed for metal additive manufacturing because physical constraints could compensate partly for sparse datasets and limited interpretability in purely data-driven models (Guo et al., 2022). Mechanistic descriptors were similarly combined with experimental observations and machine learning to rank physical variables controlling additive-manufacturing defects, demonstrating that physically meaningful features could strengthen defect prediction beyond unconstrained correlations (Du et al., 2021). ()

A second unresolved dimension was introduced when recycled feedstock was considered. AA7075 machining chips were consolidated successfully through direct hot-press forging, but mechanical integrity remained strongly dependent on processing temperature and holding time, and the route was developed for bulk consolidation rather than welding-wire production (Ruhaizat et al., 2022). Solid-state recycling of AA7075 waste reinforced with ceramic nanoparticles was also optimized through extrusion, equal-channel angular pressing, and heat treatment, through which strong interactions among processing and reinforcement variables were demonstrated (Sabbar et al., 2021). For AlMgSi chips, thermal pretreatment before direct extrusion altered alumina enrichment and final density, confirming that upstream chip condition was propagated into recycled material properties (Wagiman et al., 2020). From an environmental perspective, metal additive-manufacturing assessments showed that feedstock preparation, machine energy, post-processing, material efficiency, and recycling all contributed materially to life-cycle performance rather than being represented adequately by deposition energy alone (Gao et al., 2021). Therefore, the recycling route, wire quality, alloy recovery, deposition stability, defect population, and qualified-product yield were required to be considered as one connected manufacturing system rather than as separate material and process problems. ()

Experimental deposition, microscopy, mechanical testing, heat treatment, thermography, numerical modelling, and machine learning were the dominant approaches across the selected literature. Grain refinement and lower

crack susceptibility were generally associated with particle-assisted equiaxed solidification, whereas porosity remained strongly dependent on shielding, thermal history, particle dispersion, and feedstock condition. Data-driven studies were increasingly extended from bead geometry toward thermal prediction and defect classification, but most models were validated within restricted materials, geometries, or sensing configurations. Recycling studies were primarily concentrated on bulk chip consolidation and environmental accounting, while aluminum-WAAM studies were primarily concentrated on virgin commercial feedstock. Methodological differences in arc mode, alloy family, heat treatment, defect definition, sensor calibration, and validation strategy prevented direct transfer of quantitative limits between studies.

The overall direction of the field was shifted from isolated parameter optimization toward coupled process–structure–property analysis, in situ sensing, computational modelling, and data-assisted quality control. At the same time, circular-material processing was increasingly examined as a means of lowering primary-material dependence and embodied energy. However, these developments were largely advanced in parallel, and limited integration was established between recycled feedstock qualification, particle-assisted grain refinement, synchronized sensing, physically constrained defect prediction, structural performance, and environmental accounting.

Existing studies failed to establish a fully connected route from AA7075 machining chips to composition-controlled, particle-modified welding wire and spatially qualified WAAM structures. Recycled-AA7075 investigations were restricted principally to bulk solid-state consolidation and therefore did not resolve wire feedability, remelting losses, hydrogen pickup, TiB_2 dispersion, or arc stability (Ruhaizat et al., 2022) (Sabbar et al., 2021), while aluminum-WAAM investigations were conducted with inconsistent process windows, defect metrics, thermal histories, and post-processing routes (Langelandsvik et al., 2021) (Sinha et al., 2022). Monitoring and machine-learning frameworks were generally constrained by single or limited sensor modalities, process-specific datasets, restricted geometries, and incomplete validation under unseen conditions (Hamrani et al., 2024) (Xia et al., 2022) (Fagersand et al., 2024), while physics-informed approaches were demonstrated predominantly outside recycled 7xxx-series WAAM (Guo et al., 2022) (Du et al., 2021). Consequently, coupled attribution of feedstock history, local thermal behavior, multimodal process signatures, XCT-verified porosity, metallographically verified cracking, microstructure, mechanical anisotropy, and environmental performance remained insufficiently validated for scalable aerospace-oriented processing.

Digital traceability was therefore established from machining-chip provenance through cleaning, remelting, compositional correction, TiB_2 incorporation, wire fabrication, WAAM deposition, specimen extraction, and environmental inventory construction. Material factors and deposition variables were varied within a structured experimental framework, while thermal imaging, electrical signals, acoustic emission, visible imaging, and robot-position data were synchronized to common spatial coordinates. XCT, microscopy, EBSD, XRD, hardness, tensile, fracture, and fatigue measurements were registered to the corresponding process histories, and physics-guided descriptors were integrated with XGBoost and Gaussian-process models under held-out-build validation and uncertainty assessment. Material recovery, process energy, shielding gas, heat treatment, machining losses, and rejected production were evaluated under consistent environmental boundaries so that defect control and manufacturing sustainability were assessed within the same process chain.

The objective of the present study is to develop and validate a traceable, physics-guided, multimodal framework for manufacturing crack-resistant aerospace structures from TiB_2-modified recycled AA7075 using wire-arc additive manufacturing.

Materials and Methods

Materials

AA7075 aluminum-alloy machining chips were used as the recycled feedstock for wire production. The chips had been generated during dry and flood-lubricated milling of wrought AA7075-T6 aerospace plate stock and were segregated according to the heat number of the parent alloy before further processing. The nominal compositional window used for charge correction was defined from the AA7075 specification range, as presented in Table 2. A

primary AA7075 ingot was used as the primary-alloy reference material. High-purity aluminum, zinc, magnesium, copper, chromium, manganese, and silicon master additions were used for compositional correction after melt analysis.

Titanium diboride (TiB_2) particles were used as the ceramic grain-refining phase. The TiB_2 powder had been certified at a purity of ≥99.0% and had been supplied with a nominal particle-size range of 50–200 nm. Before use, the powder was stored in sealed desiccated containers. Argon with a certified purity of 99.999% was used for melt protection, WAAM shielding, and furnace backfilling. A commercial NaCl–KCl-based flux was used during remelting only when oxide disruption was required. Analytical-grade acetone and ethanol, an alkaline degreasing solution, and deionized water were used during feedstock cleaning. All consumables were handled under laboratory conditions maintained at 23 ± 2 °C and 50 ± 10% relative humidity (RH).

The compositional limits and analytical acceptance criteria that were applied before wire fabrication were defined as shown in Table 2.

Table 2. Nominal compositional limits and analytical acceptance criteria that were used for AA7075 feedstock correction.

Element	Target range / mass %	Analytical method	Acceptance criterion before wire fabrication
Zn	5.10–6.10	Optical emission spectroscopy and ICP-OES	Acceptance was based on compliance with the AA7075 target range
Mg	2.10–2.90	Optical emission spectroscopy and ICP-OES	Acceptance was based on compliance with the AA7075 target range
Cu	1.20–2.00	Optical emission spectroscopy and ICP-OES	Acceptance was based on compliance with the AA7075 target range
Cr	0.18–0.28	Optical emission spectroscopy and ICP-OES	Acceptance was based on compliance with the AA7075 target range
Si	≤0.40	Optical emission spectroscopy	Acceptance was based on compliance with the specified maximum
Fe	≤0.50	Optical emission spectroscopy	Acceptance was based on compliance with the specified maximum
Mn	≤0.30	Optical emission spectroscopy	Acceptance was based on compliance with the specified maximum
Ti	≤0.20, excluding TiB_2 addition	Optical emission spectroscopy	The concentration was recorded for compositional correction
Al	Balance	Calculated by difference	The remaining composition was assigned to Al

The complete experimental sequence was organized from chip segregation through feedstock preparation, wire production, deposition, synchronized monitoring, specimen extraction, and post-deposition characterization, as

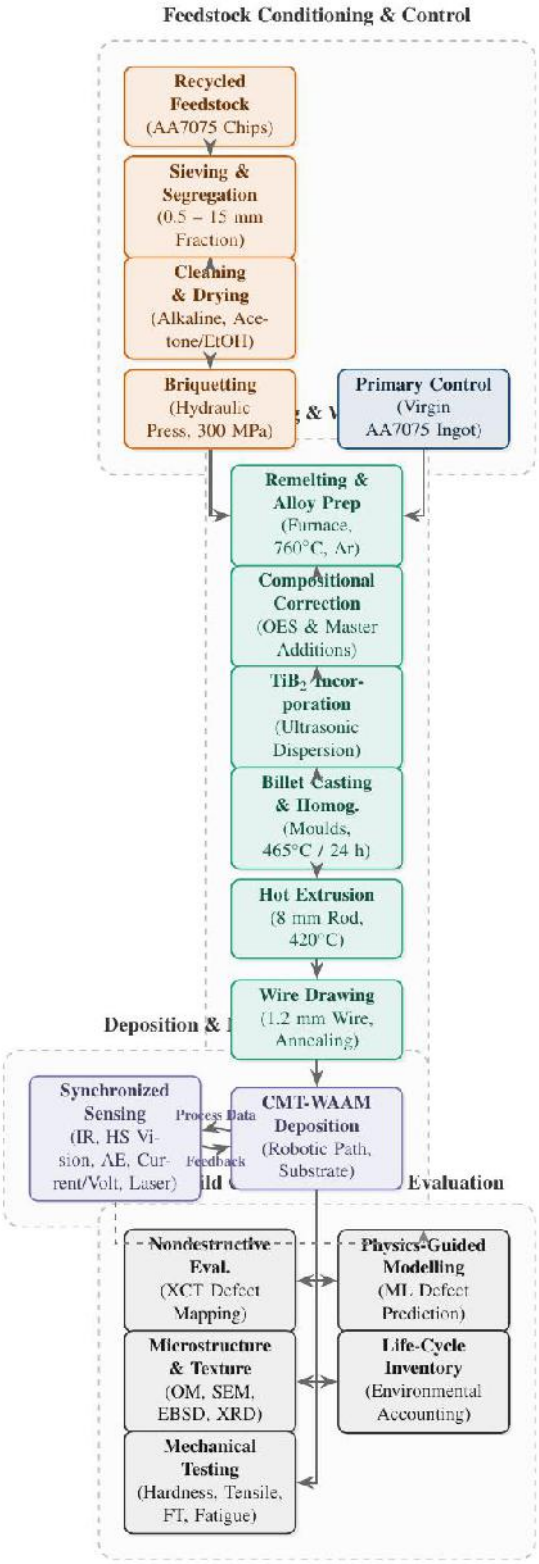

illustrated in Figure 1.

Figure 1. Experimental process flow

Feedstock Cleaning, Remelting, TiB_2 Incorporation, and Wire Fabrication

The machining chips were sieved before cleaning. Fines smaller than 0.5 mm and oversized curled chips larger than 15 mm were removed, and the remaining fraction was subjected to sequential alkaline degreasing, deionized-water rinsing, acetone washing, and ethanol rinsing. The cleaned chips were dried at 120 °C for 4 h in a forced-air oven and were transferred directly to a desiccator before melting. Residual moisture and volatile contamination were evaluated by thermogravimetric analysis from 25 to 500 °C under flowing argon. Representative chip batches were also analyzed for oxygen, hydrogen, nitrogen, and carbon before and after cleaning so that changes introduced by the cleaning sequence could be documented.

Following cleaning and drying, the recycled AA7075 chips were compacted into cylindrical briquettes at 300 MPa using a hydraulic press. The briquettes were remelted in a graphite-coated silicon-carbide crucible placed in an electric resistance furnace. A continuous argon cover-gas flow of 15 L min^{-1} was maintained during melting, and the melt temperature was controlled at 760 ± 10 °C. After a 15 min holding period had been completed, surface dross was removed mechanically.

Chill-cast pins were taken from the melt, and the chemical composition was determined by optical emission spectroscopy. Certified master additions were subsequently introduced until the composition had been brought within the acceptance window given in Table 2. After compositional correction had been completed, the melt was mechanically stirred at 300 rev min^{-1} for 5 min using a graphite impeller.

TiB_2 additions of 0.0, 0.5, 1.0, 1.5, and 2.0 mass % were incorporated to establish the particle-concentration series. Before incorporation, the TiB_2 powder was dried under vacuum at 200 °C for 2 h. The dried powder was enclosed in aluminum-foil packets and was plunged below the melt surface while mechanical stirring was maintained at 500 rev min^{-1}. Particle dispersion was further promoted by ultrasonic melt treatment at 20 kHz and 1.2 kW for 180 s. During ultrasonication, a titanium sonotrode was positioned 20 mm below the melt surface.

After TiB_2 incorporation had been completed, the melt was cast into steel molds that had been preheated to 250 °C. Billets with a diameter of 40 mm were produced. The billets were homogenized at 465 °C for 24 h under argon, were furnace-cooled to 200 °C, and were subsequently air-cooled.

The homogenized billets were hot-extruded at 420 °C using an extrusion ratio of 25:1, through which rods with a diameter of 8 mm were produced. Where additional drawability was required, the rods were solution-treated at 470 °C for 1 h. Wire drawing was then performed through tungsten-carbide dies until a final wire diameter of 1.2 ± 0.02 mm had been obtained. Intermediate annealing at 350 °C for 30 min was applied whenever the accumulated reduction in cross-sectional area had exceeded 35%.

Wire diameter was measured at 0.5 m intervals using a laser micrometer. Surface morphology was evaluated by optical profilometry, and the surface roughness was reported as the arithmetic mean height, R_a, over a scan length of 10 mm. After inspection had been completed, the wire spools were sealed in vacuum-packed aluminum barrier bags containing desiccant and were stored in that condition until deposition.

WAAM Equipment and Multimodal Instrumentation

WAAM deposition was performed using a cold metal transfer (CMT) gas-metal arc welding system integrated with a six-axis robotic motion platform. A Fronius TPS 400i CMT power source was used with a programmable wire-feed drive. Torch motion was provided by a KUKA KR 60 HA robotic manipulator with a positional repeatability of ±0.05 mm.

AA7075 substrate plates measuring 300 mm × 150 mm × 12 mm were used for wall deposition. Before deposition, the substrate surfaces were mechanically ground using 600-grit SiC paper, were degreased with acetone, and were clamped to a water-cooled steel fixture. Arc shielding was supplied using argon at 22 L min^{-1} through a standard GMAW nozzle with an internal diameter of 16 mm.

Surface temperature evolution was measured using a calibrated infrared imaging system that operated over the 3–5 µm spectral range. Thermal images were acquired at 1000 Hz. Melt-pool and arc behavior were recorded using a high-speed visible-light camera that was positioned coaxially with auxiliary illumination, and images were acquired at 5000 frames s^{-1}. Arc voltage was measured through an isolated voltage-divider circuit, whereas welding current was measured using a Hall-effect current transducer. Acoustic-emission signals were obtained

using two wideband piezoelectric sensors that were coupled to the build substrate using a high-temperature couplant. Wall geometry was additionally monitored using a laser line-profile scanner mounted on the robot end effector.

The measurement systems, operating ranges, acquisition settings, and calibration references that were used during deposition and characterization were summarized in Table 3.

Table 3. Instrumentation, acquisition settings, and calibration references that were used during WAAM deposition and subsequent characterization.

Instrument	Model / manufacturer	Measurement range	Sampling setting	Calibration reference
GMAW power source	Fronius TPS 400i CMT	0–400 A	Internal control frequency	Manufacturer calibration
Robotic manipulator	KUKA KR 60 HA	Six-axis motion	Path interpolation at 250 Hz	Laser-tracker verification
Infrared camera	FLIR X6900sc or equivalent	300–1500 °C	1000 Hz	Blackbody furnace
Visible high-speed camera	Photron FASTCAM or equivalent	Optical intensity	5000 frames s^{-1}	Spatial calibration grid
Current transducer	LEM closed-loop Hall sensor	0–500 A	20 kHz	Precision current source
Voltage divider	Isolated differential divider	0–60 V	20 kHz	Calibrated digital multimeter
Acoustic-emission sensors	Physical Acoustics wideband sensors	100–900 kHz	2 MHz	Pencil-lead break and pulser
Laser profile scanner	Micro-Epsilon scanCONTROL or equivalent	±25 mm	200 Hz	Gauge-block artifacts
X-ray computed tomography	Nikon XT H 225 or equivalent	0–225 kV	Voxel size was recorded for each scan	Certified dimensional artifact
SEM/EBSD	FEI Quanta 650 FEG or equivalent	0.5–30 kV	Step size was selected for each specimen	Silicon standard
Universal testing machine	Instron 5982 or equivalent	0–100 kN	10 Hz	ISO-traceable load cell

The WAAM cell was configured so that the torch, substrate, clamping fixture, thermal camera, visible camera, acoustic-emission sensors, electrical measurement system, laser scanner, and data-acquisition computer could be operated simultaneously. Line-of-sight measurement was maintained for the optical systems, and electrical

isolation was maintained between the welding circuit and sensing hardware, as represented in Figure 2.

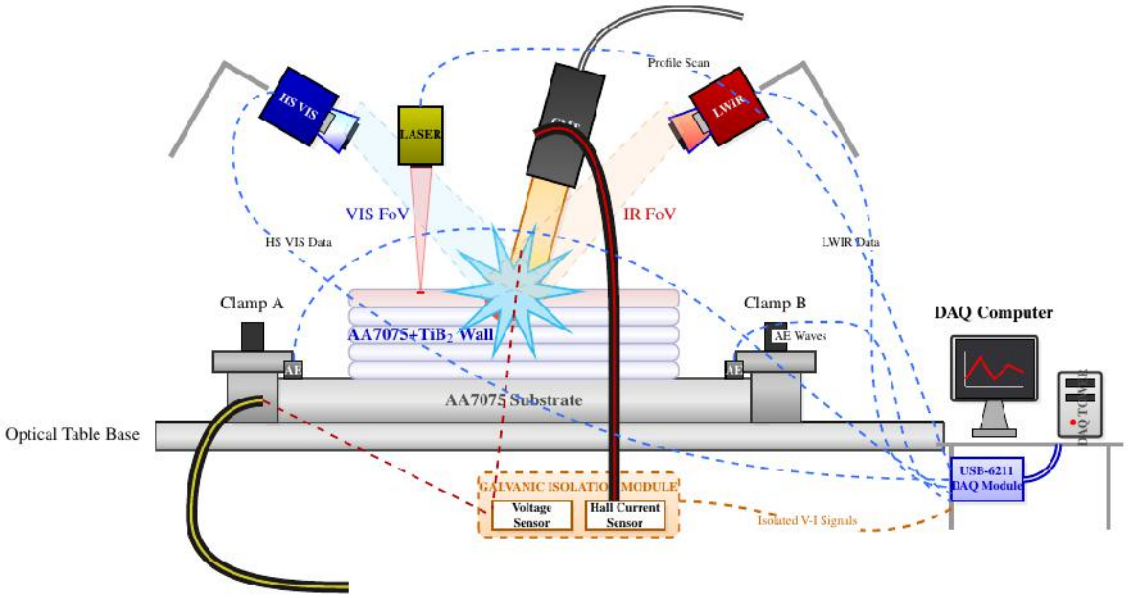

Figure 2. WAAM deposition cell in which the torch, substrate, clamping system, thermal and visible cameras, acoustic-emission sensors, electrical-signal acquisition system, laser scanner, and synchronized data-acquisition hardware were arranged.

Experimental Setup, Deposition Conditions, and Process Window

Single-bead trials and multilayer wall builds were fabricated before specimen extraction so that deposition stability, thermal-history control, and geometric development could be evaluated. A nominal wall length of 120 mm and a target wall height of 40 mm were used. A unidirectional interlayer path was programmed unless another path condition had been specified in the experimental design.

The contact-tip-to-work distance was maintained at 12 ± 1 mm, and the torch was held at 90° relative to the substrate surface. Shielding-gas flow was initiated 10 s before arc ignition and was maintained for 20 s after arc extinction.

The process space was investigated through a structured experimental design in which wire-feed rate, travel speed, welding current, arc voltage, interpass temperature, and TiB_2 concentration were varied within the ranges given in Table 4. Shielding-gas flow and contact-tip-to-work distance were held constant.

Interpass temperature was measured at the centerline of the previously deposited layer using infrared thermography. Periodic verification was performed using a contact thermocouple attached near the wall base. Deposition of each subsequent layer was initiated only after the prescribed interpass temperature had been reached. Laboratory temperature and relative humidity were logged continuously throughout all builds.

Table 4. WAAM process factors and experimental ranges that were applied during deposition.

Factor	Symbol	Unit	Prescribed range	Control mode
Wire-feed rate	v_f	m min^{-1}	3.0–7.0	Power-source controlled
Travel speed	v_t	mm s^{-1}	4.0–10.0	Robot controlled
Mean welding current	I	A	80–160	Synergic CMT setting
Mean arc voltage	V	V	12–22	Synergic CMT setting

Factor	Symbol	Unit	Prescribed range	Control mode
Interpass temperature	T_i	°C	80–180	Dwell-time controlled
TiB_2 concentration	C_{TiB_2}	mass %	0.0–2.0	Feedstock controlled
Shielding-gas flow rate	Q_g	L min^{-1}	22	Fixed
Contact-tip-to-work distance	d_{ctwd}	mm	12 ± 1	Fixed

The nominal heat input per unit length was calculated from the measured electrical signals and travel speed according to Equation (1):

$$H = \frac{\eta V I}{v_t} \qquad (1)$$

where $H$was defined as the nominal heat input per unit length in J mm^{-1}, $\eta$was defined as the process thermal efficiency, $V$was defined as the time-averaged arc voltage in V, $I$was defined as the time-averaged welding current in A, and $v_t$was defined as the travel speed in mm s^{-1}. A constant thermal-efficiency value was used for comparative process calculations, and the selected value was documented with the corresponding build record. For signal-level analyses, time-resolved heat input was additionally calculated from the synchronized instantaneous voltage and current signals.

Sensor Calibration, Synchronization, and Experimental Traceability

All measurement systems were calibrated before specimen fabrication was undertaken. The infrared camera was calibrated against a blackbody source over a temperature interval of 300–1200 °C. Surface emissivity was determined using representative AA7075 surfaces that had been prepared with grinding and oxidation conditions corresponding to those of the deposited material.

The visible camera was spatially calibrated using a certified grid target positioned at the build-plane height. The current transducer was calibrated with a precision current source over 0–300 A, and the isolated voltage-divider circuit was calibrated against a digital multimeter traceable to national standards. Acoustic-emission sensor response was verified before each build by pencil-lead break tests performed at three locations on the substrate. The laser profile scanner was calibrated using gauge blocks and a stepped-height artifact.

Temporal synchronization was established using a common hardware trigger generated at arc initiation. The trigger signal was recorded simultaneously by the infrared camera, high-speed visible camera, electrical-signal acquisition system, acoustic-emission system, and robot controller. All timestamps were stored in Coordinated Universal Time with millisecond precision.

Spatial registration was established by transformation of the robot tool-center-point coordinates into the build coordinate system using a three-point substrate reference frame. Calibration records, raw sensor files, processed datasets, build coordinates, feedstock records, and specimen identifiers were linked through a common build-identification code. The traceability structure through which each material batch and test specimen was linked to its corresponding process history was organized as shown in Figure 3.

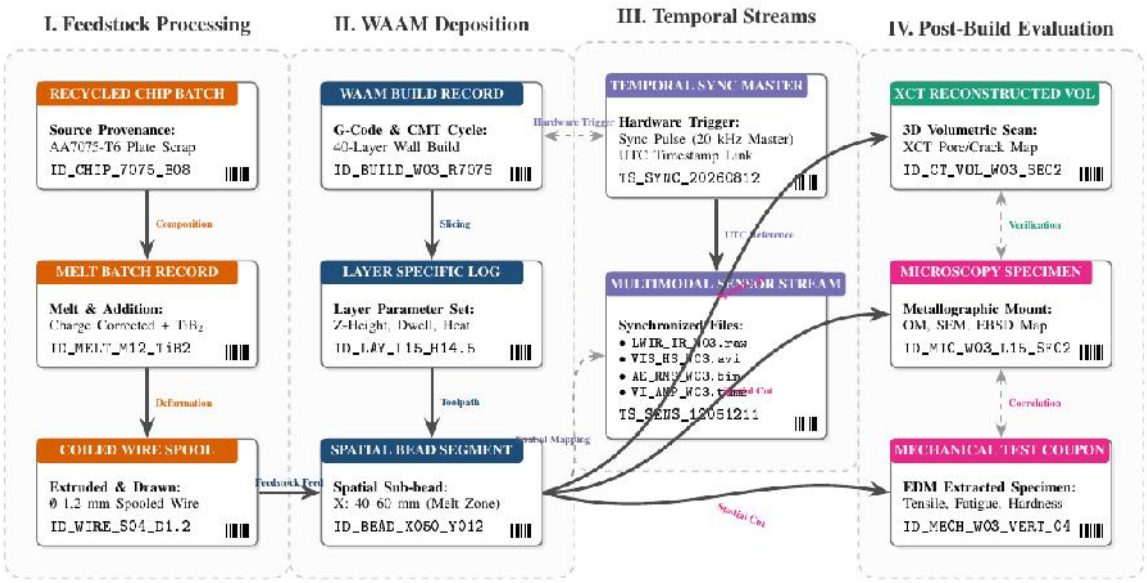

Figure 3. Calibration, synchronization, and traceability architecture

In Situ Sensing and Measurement Procedures

Infrared thermography was used for measurement of surface-temperature fields during deposition. The thermal camera was positioned at 35° relative to the substrate normal and at a distance of 0.75 m from the wall centerline. Reflected arc radiation was reduced through optical filtering, and saturated pixels were excluded from the thermal analysis. A thermal region of interest encompassing the molten pool, trailing solidification region, and previously deposited material within 20 mm of the arc was used. Cooling histories were extracted at fixed spatial coordinates after passage of the heat source.

Electrical signals were acquired directly from the welding circuit. Arc voltage was measured between the contact tip and the substrate fixture, whereas welding current was measured on the power-source return cable. Both signals were digitized at 20 kHz using a 16-bit data-acquisition system.

The two acoustic-emission sensors were positioned 40 and 100 mm from the wall start location along the substrate centerline. A preamplifier gain of 40 dB was applied, and the signals were band-pass filtered over 100–900 kHz before digitization at 2 MHz.

High-speed visible imaging was used for determination of melt-pool length, melt-pool width, leading-edge position, and arc position relative to the programmed tool path. Laser profilometry was performed after every fifth deposited layer and again after final cooling so that layer-height development and final wall geometry could be documented before destructive specimen extraction.

Ray Computed Tomography and Defect Quantification

X-ray computed tomography (XCT) was used for volumetric mapping of internal defects. Specimens were scanned at 120–180 kV and 80–150 µA. The reconstructed voxel size was selected according to specimen thickness and was documented for each dataset. Beam-hardening and ring-artifact corrections were applied consistently across corresponding scans.

Pores and cracks were segmented using documented threshold-based and morphological procedures. The minimum reportable defect dimension was defined relative to the reconstructed voxel size, with a general detection limit corresponding to three times the voxel-edge length. For the spatially registered wall reconstruction used for defect mapping, a reconstructed voxel size of 35 µm was applied; a minimum three-voxel threshold was applied to pore detection, whereas a minimum ten-voxel threshold was applied to crack detection.

Volumetric porosity was calculated from the segmented XCT data according to Equation (3). Before that calculation was performed, all segmented objects below the defined detection threshold were excluded.

$$P_v = \frac{\sum_{i=1}^{n} V_{p,i}}{V_s} \times 100 \qquad (3)$$

where P_v was defined as volumetric porosity in %, $V_{p,i}$ was defined as the volume of the i^{th} segmented pore in mm³, n was defined as the number of segmented pores, and V_s was defined as the analyzed specimen volume in mm³. The segmentation threshold, reconstructed voxel size, and minimum defect volume were documented for each XCT dataset.

Hot-crack density was quantified from the registered XCT and metallographic observations according to Equation (4):

$$\rho_c = \frac{\sum_{j=1}^{m} l_{c,j}}{A_s} \qquad (4)$$

where ρ_c was defined as crack density in mm mm^{-2}, $l_{c,j}$ was defined as the projected length of the j^{th} detected crack in mm, m was defined as the number of identified cracks, and A_s was defined as the analyzed section area in mm². Only cracks that exceeded the predefined detection limits were included in the calculation.

Metallography, SEM, EBSD, and X-Ray Diffraction

Metallographic specimens were extracted from the start, middle, and end regions of each wall. The sections were mounted in conductive resin and were ground sequentially using SiC papers from P320 to P4000. Polishing was then performed using diamond suspensions down to 1 µm, after which final polishing was completed using colloidal silica.

Where grain-boundary contrast was required for optical microscopy, Keller-type etching was applied. SEM and electron backscatter diffraction (EBSD) measurements were performed on unetched polished surfaces. EBSD maps were acquired at an accelerating voltage of 20 kV and a working distance of 15–20 mm. The step size was selected so that at least ten measurement points were obtained across the smallest expected grain dimension. For the representative recycled AA7075 specimen containing 1.0 mass % TiB_2 that was used for through-height texture and grain-structure analysis, a step size of 0.5 µm was applied.

Grain reconstruction was performed after unindexed points and grains below the predefined minimum pixel-count criterion had been removed. Equivalent-circle diameter was used for grain-size quantification. Grain aspect ratio, equiaxed-grain fraction, crystallographic texture intensity, and kernel average misorientation were extracted from the reconstructed maps. Texture was represented using inverse-pole-figure maps and orientation-distribution functions.

Particle distribution was quantified from SEM backscattered-electron micrographs. Contrast-based segmentation was applied, after which segmented particle populations and agglomerates were manually verified. Particle size, number density, agglomerate fraction, and particle–matrix spatial descriptors were thereby obtained.

Phase characterization was performed by X-ray diffraction using Cu Kα radiation over a 2θ range of 20–100°.

Mechanical Testing and Spatial Registration of Test Specimens

Mechanical-test specimens were removed by electrical-discharge machining from documented wall coordinates. Where wall geometry permitted, specimens were extracted along the build, travel, and transverse directions so that orientation-dependent properties could be evaluated.

Sub-size flat tensile specimens with a nominal gauge length of 25 mm were prepared. Hardness was mapped using Vickers indentation with a test force of 0.98 N and a dwell time of 10 s. Fracture-toughness and fatigue specimens were extracted only after nondestructive inspection had been completed, and their build coordinates were documented before machining.

All mechanical tests were performed under laboratory conditions of 23 ± 2 °C and 50 ± 10% RH. Specimen dimensions were measured at three positions within the gauge region before testing. Load cells and extensometers were verified before each test series. After fracture and fatigue testing had been completed, the fracture surfaces were preserved in labeled desiccated containers for subsequent SEM examination.

Data Acquisition, Signal Conditioning, and Feature Extraction

Raw data were stored without lossy conversion. Infrared measurements were stored as radiometric thermal data, visible-camera measurements were stored as timestamped image sequences, and electrical and acoustic-emission measurements were stored as binary waveform files. Robot position, commanded travel speed, wire-feed command, shielding-gas status, and power-source state were exported from the controller log after each build.

Following temporal synchronization, the process variables were resampled onto a common time base to produce a unified process table. Because substantially higher sampling rates had been used for acoustic-emission measurements, acoustic descriptors were first calculated over moving time windows and were subsequently registered with the lower-frequency process variables.

Electrical signals were conditioned using a zero-phase finite-impulse-response low-pass filter with a cutoff frequency of 2 kHz for process-state analysis. Acoustic-emission signals were band-pass filtered between 100 and 900 kHz. Thermal images were corrected for background radiation, surface emissivity, and camera viewing geometry. Melt-pool boundaries were segmented from visible-light images by intensity thresholding followed by morphological closing. All thresholds and processing parameters were stored with the associated build metadata.

An average temperature-change rate over a predefined cooling interval was calculated from the registered thermal history according to Equation (2):

$$T_{\Delta T} = \frac{T_2 - T_1}{t_2 - t_1} \qquad (2)$$

where $T_{\Delta T}$ was defined as the average temperature-change rate during cooling in °C s^{-1}, T_1 and T_2 were defined as the upper and lower temperatures of the selected interval in °C, respectively, and t_1 and t_2 were defined as their corresponding times in s. The same temperature interval was applied to all specimens included within a given model-training dataset.

Experimental Design and Microstructural Response Variables

A mixed factorial and response-surface design was used. TiB_2 concentration and recycled-content condition were treated as material factors, whereas wire-feed rate, travel speed, welding-current setting, and interpass temperature were treated as process factors. Replicate builds were assigned to selected center-point conditions so that experimental repeatability could be estimated. Build order was randomized within the practical restrictions imposed by wire-spool replacement and furnace-batch preparation.

The experimental blocks, replication strategy, and primary measurements that were used throughout the study were organized as shown in Table 5.

Table 5. Design-of-experiments structure that was used for feedstock preparation, deposition, sensing, characterization, mechanical testing, and predictive-model validation.

Experimental block	Material condition	Process factors	Replication strategy	Primary measurements
Feedstock block	Primary and recycled AA7075 with TiB_2 levels	Melt route, correction route, wire-drawing sequence	A minimum of three wire sections was sampled from each spool	Chemistry, H/O/C/N content, roughness, TiB_2 dispersion
Single-bead block	Selected wire conditions	v_f, v_t, I, V, T_i	Center-point conditions were repeated	Bead geometry, thermal history, signal stability
Wall-build block	Selected stable wire conditions	v_f, v_t, I, T_i, C_{TiB_2}	Build-level replication was performed	XCT, EBSD, hardness, sensor features

Experimental block	Material condition	Process factors	Replication strategy	Primary measurements
Mechanical block	Extracted wall specimens	Orientation and build location	The required number of valid specimens was obtained for each condition	Tensile response, hardness, fracture behavior, fatigue response
Modeling block	Spatially registered process–structure dataset	Sensor features and physics-guided descriptors	Leave-one-build-out validation was performed	Defect labels and uncertainty metrics

Microstructural response variables were obtained from the registered microscopy and EBSD datasets. Grain size, grain aspect ratio, equiaxed-grain fraction, crystallographic texture intensity, kernel average misorientation, and particle-agglomeration descriptors were quantified. Grain size was calculated from equivalent-circle diameters after removal of unindexed pixels and grains below the established reconstruction threshold. Particle dispersion was quantified using contrast-segmented backscattered-electron micrographs after manual verification of the segmented regions.

Physics-Guided Machine-Learning Framework

Machine-learning datasets were generated by spatial division of each deposited wall into registered bead segments. Each segment was assigned its corresponding process settings, thermal-history descriptors, electrical descriptors, acoustic-emission descriptors, visible melt-pool descriptors, robot-position information, feedstock chemistry, and ex situ defect labels. XCT-defined porosity, registered crack measurements, and EBSD-derived microstructural descriptors were used as ground-truth outputs where applicable.

XGBoost regression and classification models were trained for deterministic point prediction. Gaussian-process regression and Gaussian-process classification were used for probabilistic predictions and uncertainty estimation. Input variables were standardized using scaling parameters derived exclusively from the training data. Hyperparameters were selected through nested cross-validation.

Generalization between deposition runs was assessed by leave-one-build-out validation. During each validation cycle, all observations associated with the held-out build were excluded from model fitting, feature standardization, and hyperparameter selection.

Before model training was performed, physics-guided descriptors were derived from the synchronized measurements. These descriptors included nominal heat input, instantaneous electrical power, interpass temperature, cooling-rate descriptors, cumulative thermal exposure, layer number, build height, local bead geometry, wire-feed-to-travel-speed ratio, and feedstock-composition descriptors.

The wire-feed-to-travel-speed ratio was calculated after consistent unit conversion according to Equation (5):

$$R_{wv} = \frac{v_f}{v_t} \qquad (5)$$

where $R_{wv}$was defined as the dimensionless wire-feed-to-travel-speed ratio, $v_f$was defined as the wire-feed rate after conversion to mm s^{-1}, and $v_t$was defined as the travel speed in mm s^{-1}. The same unit conversion was applied to all observations before model training.

Classification performance was evaluated using accuracy, precision, recall, F1 score, receiver-operating-characteristic area, and probability-calibration error. Regression performance was evaluated using mean absolute error, root-mean-square error, coefficient of determination, and prediction-interval coverage. Feature contributions were evaluated after model training using permutation importance and SHAP values.

Statistical comparisons among experimental groups were performed using analysis of variance when the required assumptions had been satisfied. Non-parametric alternatives were used when those assumptions had not been met.

Normality was evaluated using the Shapiro–Wilk test, and homogeneity of variance was evaluated using Levene's test. Statistical significance was assessed at

$$\alpha = 0.05.$$

The complete pathway through synchronization, spatial registration, feature extraction, physics-guided descriptor construction, ex situ labeling, model fitting, and held-out-build validation was organized as shown in Figure 4.

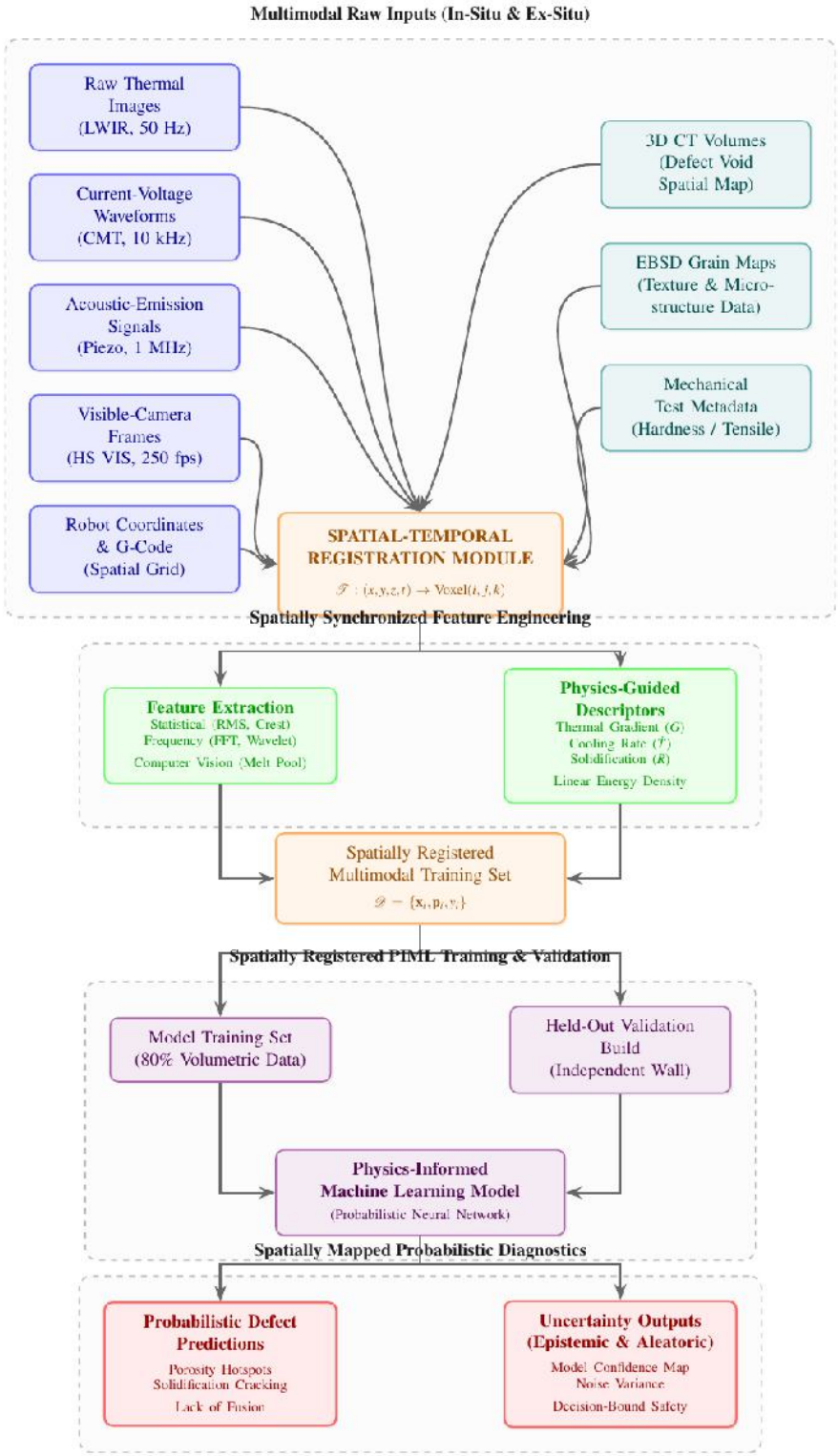

Figure 4. Data-processing and physics-guided machine-learning workflow

Measurement and Prediction Uncertainty

Measurement uncertainty was evaluated for chemical composition, wire diameter, infrared thermography, electrical measurements, acoustic-emission timing, XCT segmentation, microstructural measurements, specimen dimensions, load measurement, and displacement measurement. Calibration uncertainty, instrument resolution, repeatability, and operator-dependent segmentation uncertainty were included where they were applicable. Unless otherwise specified, expanded uncertainty was reported using a coverage factor of

$$k = 2.$$

For quantities calculated from multiple measured variables, standard uncertainty was propagated using the root-sum-square formulation given in Equation (6):

$$u_y = \sqrt{\sum_{i=1}^{q} \left(\frac{\partial f}{\partial x_i} u_{x_i}\right)^2} \qquad (6)$$

where $u_y$was defined as the combined standard uncertainty associated with the calculated quantity $y = f(x_1, x_2, \ldots, x_q)$, $x_i$was defined as the i^{th}input variable, $u_{x_i}$was defined as the standard uncertainty associated with x_i, and $q$was defined as the total number of input variables. Input variables were treated as independent unless covariance had been identified from the corresponding calibration or acquisition records.

For nonlinear calculated quantities and segmented-image measurements, uncertainty propagation was performed through Monte Carlo perturbation of the input variables within their assigned uncertainty distributions.

Where the probabilistic model structure permitted separation, predictive uncertainty was partitioned into model and observation components. Prediction intervals were calculated for regression outputs, whereas calibrated probability intervals were calculated for classification outputs. Probability calibration was evaluated using reliability diagrams and expected calibration error. Uncertainty estimates were not transferred between material batches unless the corresponding feedstock descriptors had been included among the model inputs.

Material-Efficiency and Environmental Assessment

A cradle-to-gate assessment was performed for three manufacturing routes: conventional primary-AA7075 production, primary-wire WAAM, and recycled-chip-to-wire WAAM. An identical functional unit of 1 kg of qualified WAAM material was applied to the compared routes.

For the recycled route, the system boundary was extended from receipt of AA7075 machining chips through cleaning, drying, briquetting, argon remelting, chemical correction, TiB_2 addition, ultrasonic melt treatment, billet casting, extrusion, wire drawing, WAAM deposition, heat-treatment operations where applicable, machining, inspection, and production of the qualified specimen. Material inputs and losses associated with dross and oxidation, melting, wire fabrication, build rejection, machining, and process handling were recorded within the route inventory. Shielding-gas use and process energy consumption were included within the same boundary.

Material recovery was determined from the recorded material inputs, process losses, and qualified output mass. Cumulative energy demand and global-warming potential were evaluated from the compiled route inventory under consistent functional-unit and system-boundary definitions.

Environmental sensitivity was evaluated by perturbation of the principal material-efficiency and process-yield variables used in the inventory. Recovery yield was varied by ±10%, the rejected-build fraction was varied by five percentage points, machining allowance was varied by ±20%, TiB_2 addition was varied by ±50%, and wire-fabrication yield was varied by ±10%. The resulting changes in cumulative energy demand and global-warming potential were evaluated relative to the corresponding base case.

Validation, Quality Assurance, and Data Reproducibility

Quality assurance was maintained through feedstock traceability, measurement calibration, replicated measurements, process-control checks, and independent verification of selected characterization procedures. Unique alphanumeric identifiers were assigned to every chip batch, melt batch, wire spool, WAAM build, sensor

record, XCT scan, metallographic mount, EBSD map, and mechanical-test specimen. The assigned identifiers were propagated through raw-data filenames, machine logs, processed datasets, and laboratory records.

Three wire regions corresponding to the beginning, middle, and end of each spool were sampled for diameter measurement, surface inspection, chemical analysis, and TiB_2-distribution assessment. Before multilayer wall fabrication was performed, trial depositions were completed so that wire feeding, arc initiation, shielding-gas delivery, and sensor synchronization could be verified.

Builds affected by shielding interruption, wire-feed interruption, sensor-trigger failure, or incomplete metadata were excluded from machine-learning model training, and each exclusion was documented in the experimental record.

XCT segmentation repeatability was evaluated by repeated segmentation of selected volumes, and the resulting defect classifications were compared with metallographic sections removed from spatially registered locations. EBSD data quality was evaluated from indexing quality, pattern quality, and the grain-reconstruction criteria applied after data cleaning.

Mechanical-specimen dimensions were measured at three positions within the gauge region before testing. Load cells and extensometers were verified before each mechanical-test series. Following testing, fracture surfaces were preserved in labeled desiccated containers until SEM characterization had been performed.

Raw experimental data were stored without overwriting. Processed datasets were version-controlled so that the complete transformation from raw measurements to analytical outputs could be traced. Signal processing, image analysis, statistical analysis, and machine-learning procedures were executed using Python 3.11 together with scikit-learn, XGBoost, GPyTorch, NumPy, Pandas, and SciPy, and MATLAB R2024b was used where applicable. Software versions, random seeds, preprocessing operations, hyperparameter-search spaces, and training, validation, and test partitions were recorded for each analytical run.

Results and Discussion

Process-Window Definition, Deposition Stability, and Bead Geometry

The combined effects of wire-feed rate, travel speed, welding current, interpass temperature, and TiB_2 concentration on WAAM process stability and geometric response were evaluated across the prescribed experimental domain. The resulting process window, representative electrical signals, thermal-response surface, and bead-geometry maps were summarized in Figure 5.

Figure 5. (a) Multivariable WAAM design space defined by wire-feed rate, travel speed, welding current, interpass temperature, TiB_2 concentration, and nominal heat input; (b) synchronized current, voltage, instantaneous power, and commanded wire-feed signals recorded during representative layer 18; (c) heat-input and interpass-temperature response map obtained at 120 A and 1.0 mass% TiB_2; and (d) bead-width, layer-height, and wall-waviness response maps obtained after deposition.

As shown in Figure 5a, the deposition space was evaluated over wire-feed rates of 3.0–7.0 m min^{-1}, travel speeds of 4.0–10.0 mm s^{-1}, welding currents of 80–160 A, interpass temperatures of 80–180 °C, and TiB_2 concentrations of 0–2.0 mass%. Nominal heat inputs of approximately 0.6–2.0 J mm^{-1} were generated within this domain. Higher heat input was associated primarily with increased wire-feed rate and welding current, reduced travel speed, and elevated interpass temperature. Considerable interaction among these variables was therefore established, and comparable heat-input levels were produced through different combinations of electrical power and travel speed. The selected validation condition was positioned near the central region of stable deposition at a wire-feed rate of approximately 5.7 m min^{-1}, a travel speed of approximately 5.8 mm s^{-1}, a current of 120 A, an interpass temperature of 120 °C, and a TiB_2 concentration of 1.0 mass%.

Process stability was further assessed from synchronized electrical and wire-feed signals recorded during representative layer 18, as presented in Figure 5b. Over six consecutive beads, the mean current was maintained at approximately 135–145 A, while the voltage was maintained at approximately 11–14 V. The corresponding instantaneous power was concentrated near 3.0 kW. The commanded wire-feed rate remained close to 4.0 m min^{-1} over most of the acquisition interval. Short reductions were detected near approximately 20, 30, 40, and 50 s and coincided with localized changes in current, voltage, and power. These disturbances were associated with bead

transitions, arc initiation or termination, and robot deceleration rather than sustained arc instability. Progressive electrical drift was not observed over the 60 s acquisition period, which indicated that wire delivery and arc-length control had been reproducible under the representative condition.

The combined effects of wire-feed rate and travel speed on heat accumulation were resolved more clearly in Figure 5c. At 120 A and 1.0 mass% TiB_2, the nominal heat input increased from approximately 0.4–0.8 J mm^{-1} at travel speeds of 8–10 mm s^{-1} to approximately 1.8–2.0 J mm^{-1} at travel speeds of 4–5 mm s^{-1} when wire-feed rates above approximately 5.5 m min^{-1} were applied. A comparatively steep heat-input gradient was produced when the travel speed fell below approximately 6 mm s^{-1}, whereas a flatter response was obtained at higher travel speeds.

The interpass-temperature contours were shifted toward higher values as wire-feed rate increased. Temperatures approaching 180 °C were associated with combinations of high deposition rate and low travel speed, whereas approximately 80–120 °C was maintained through intermediate parameter combinations. The selected validation condition was located near a nominal heat input of approximately 1.2–1.4 J mm^{-1} and between the 100 and 120 °C interpass-temperature contours. Excessive thermal accumulation was therefore avoided without displacement into the low-energy region in which incomplete spreading or fusion had been associated with insufficient deposited-energy density.

The bead-geometry response shown in Figure 5d was governed strongly by the balance between deposited wire volume and torch translation. Bead width increased from approximately 6 mm at a wire-feed rate of 3 m min^{-1} and a travel speed of 10 mm s^{-1} to approximately 14 mm at 7 m min^{-1} and 4–5 mm s^{-1}. Layer height increased concurrently from approximately 0.5 to 3.0 mm. The largest dimensional gradients were generated when travel speed was reduced below approximately 6 mm s^{-1}, where the deposited material volume per unit path length increased markedly.

Wall waviness remained below approximately 0.4 mm at wire-feed rates of 3–4 m min^{-1} and travel speeds of 4–7 mm s^{-1}. In contrast, waviness values approaching 1.6–2.0 mm were obtained at higher wire-feed rates, particularly when elevated travel speed was imposed simultaneously. This behavior was associated with insufficient lateral redistribution of the increased deposited volume and with subsequent amplification of local layer-height deviations during sequential deposition. A process region centered at approximately 5–6 m min^{-1} wire-feed rate and 5–7 mm s^{-1} travel speed was consequently identified as the most balanced region for deposition rate, geometric consistency, bead continuity, and thermal management.

The process-window analysis therefore demonstrated that nominal heat input alone did not fully describe deposition quality. Equivalent energy levels had been generated through different combinations of wire addition and travel speed, yet different bead dimensions and thermal histories had been produced. Process qualification was therefore strengthened when electrical stability, interpass temperature, deposition-volume balance, and geometric response were considered together rather than as isolated variables.

Spatial Distribution and Morphology of Porosity and Hot Cracking

Internal defects were evaluated through spatially registered X-ray computed tomography and metallographic analysis. The reconstructed defect field, porosity distribution, crack-density distribution, and defect-morphology statistics were summarized in Figure 6.

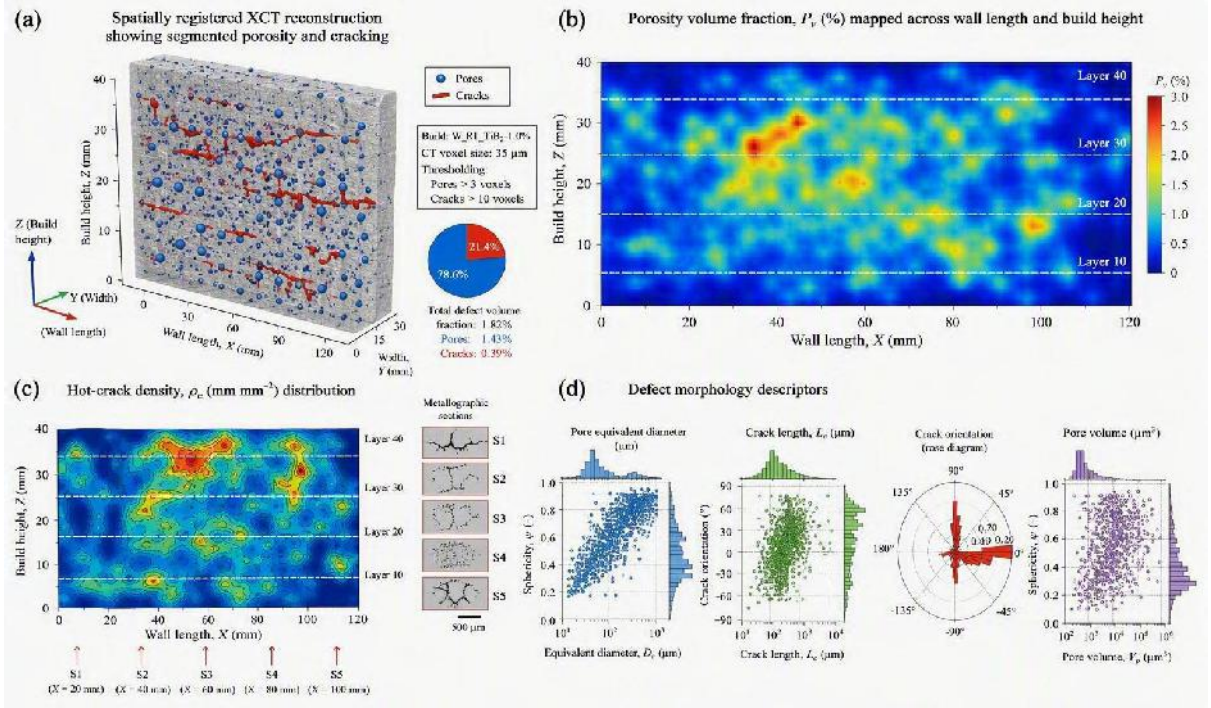

Figure 6. (a) Spatially registered XCT reconstruction of segmented pores and cracks throughout the WAAM wall; (b) porosity-volume-fraction distribution as a function of wall length and build height; (c) registered hot-crack-density field with corresponding metallographic sections; and (d) distributions of pore equivalent diameter, pore sphericity, crack length, crack orientation, and pore volume.

A spatially registered XCT reconstruction was produced for the 120 mm-long and 40 mm-high wall, as shown in Figure 6a. A reconstructed voxel size of 35 µm was used. Minimum detection thresholds of three voxels for pores and ten voxels for cracks were applied. Under these conditions, the total detectable defect volume fraction was measured as 1.82%. Porosity accounted for 1.43%, whereas cracking accounted for 0.39%. Consequently, 78.6% of the segmented defect volume was represented by pores and 21.4% was represented by cracks.

Pores were distributed throughout the wall, although larger individual defects and pore clusters were concentrated preferentially within the middle and upper build regions. Cracks were less numerous but extended over greater distances and exhibited greater spatial connectivity than the pores. Approximately horizontal crack populations were repeatedly observed near several layer bands. Their spatial arrangement was consistent with the influence of reheating, interlayer restraint, and continuity of terminal liquid films during sequential solidification, mechanisms that had also been identified as important in deposited metallic structures (S. et al., 2024).

The porosity field shown in Figure 6b varied from approximately 0 to 3.0%. Regions containing less than approximately 0.5% porosity were measured near parts of the wall boundaries and within the lower build region. Local maxima of approximately 2.0–3.0% were identified at wall coordinates of approximately $X = 35$–50 mm and $Z = 25$–31 mm, $X = 55$–65 mm and $Z = 18$–22 mm, and $X = 95$–102 mm and $Z = 12$–15 mm. Intermediate porosity levels of approximately 1.0–1.8% were distributed across several regions corresponding approximately to layers 20–35.

A simple monotonic increase in porosity with build height was not observed. Instead, discrete pore clusters were superimposed on the broader thermal history generated during wall growth. This spatial behavior was associated with localized variations in hydrogen supersaturation, oxide entrainment, melt-pool dimensions, and the time available for gas escape before solidification. The absence of a strictly height-dependent trend also indicated that local process transients had contributed substantially to pore formation.

A more continuous spatial distribution was observed for hot cracking, as shown in Figure 6c. Pronounced crack-density bands were measured at build heights of approximately $Z = 16$–18 mm and $Z = 30$–35 mm. The greatest

intensity within the upper band was concentrated near $X = 45$–65 mm, while secondary maxima were observed near $X = 85$–100 mm.

Metallographic sections S1–S5 were used to verify the registered XCT features. Branched and interconnected cracks were confirmed in the corresponding locations rather than chains of closely spaced pores. More extensive crack branching was observed at S1, S2, S3, and S5, whereas a lower crack population was measured at S4. These spatial differences demonstrated that hot cracking had not been governed by nominal composition alone. Variations in local thermal accumulation, contraction restraint, solidification direction, and interactions with neighboring defects were also implicated.

Defect morphology was quantified in Figure 6d. Pore equivalent diameters extended from approximately 10 to 10^3 μm, with most pores concentrated between approximately 30 and 200 μm. Pore sphericity generally increased with equivalent diameter, although substantial scatter was measured. Small pores exhibited sphericities from approximately 0.2 to 0.8, whereas many pores above 100 μm exhibited values between approximately 0.5 and 0.9.

Crack lengths extended from approximately 10 μm to nearly 10^4 μm, with the principal population distributed between approximately 10^2 and 10^3 μm. Preferential crack orientations were measured close to 0° and 90°, with the strongest population centered near 0°. Directional alignment with the wall and deposited-layer orientations was therefore established. Pore volumes ranged from approximately 10^2 to 10^6 μm³, and the largest pores generally exhibited intermediate-to-high sphericity.

The simultaneous occurrence of comparatively rounded pores and directionally extended cracks supported the operation of distinct defect-formation mechanisms. Gas entrapment and shrinkage-related pore formation were differentiated morphologically from solidification-induced separation, although the same evolving thermal and process environment influenced both defect populations. The spatial registration of these defect classes was therefore considered important for subsequent correlations with sensor signatures and local mechanical behavior.

TiB_2 Dispersion, Grain Refinement, Texture, and Local Misorientation

The effect of TiB_2 addition on particle distribution and solidification microstructure was evaluated using electron microscopy, elemental mapping, and EBSD. Particle-scale observations, through-height grain morphology, quantitative grain statistics, texture intensity, and kernel average misorientation were summarized in Figure 7.

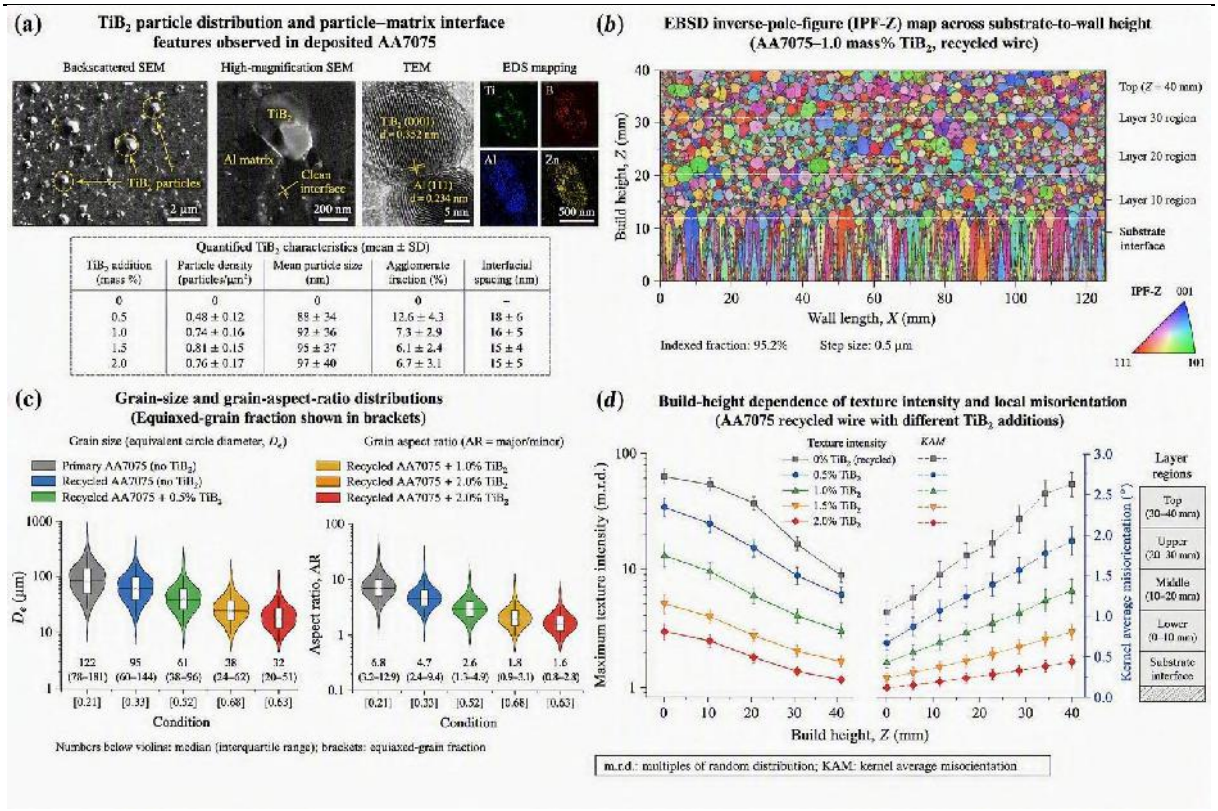

Figure 7. (a) TiB_2 particle distribution, particle–matrix interfaces, lattice fringes, elemental maps, and quantified particle characteristics; (b) EBSD IPF-Z map from the substrate interface to the upper wall region for recycled AA7075 containing 1.0 mass% TiB_2; (c) grain-size and grain-aspect-ratio distributions with corresponding equiaxed-grain fractions; and (d) build-height dependence of crystallographic texture intensity and kernel average misorientation.

TiB_2 particles were detected throughout the deposited AA7075 matrix by backscattered-electron microscopy, high-magnification SEM, TEM, and elemental mapping, as shown in Figure 7a. A clean particle–matrix interface was observed. Lattice spacings of 0.352 and 0.234 nm were assigned to TiB_2 (0001) and Al (111), respectively. Co-localized Ti and B signals confirmed the ceramic-particle identity, while the Al matrix and Zn-enriched regions were resolved independently.

Particle number density increased substantially with TiB_2 addition. Values of 0.48 ± 0.12 particles μm^{-2} at 0.5 mass%, 0.74 ± 0.16 particles μm^{-2} at 1.0 mass%, and 0.81 ± 0.15 particles μm^{-2} at 1.5 mass% were measured. At 2.0 mass%, a slight decrease to 0.76 ± 0.17 particles μm^{-2} was observed despite the larger nominal ceramic addition. This reduction was associated with increased particle association and with reduced separation of closely spaced particles during image-based counting.

The mean particle size increased moderately from 88 ± 34 nm at 0.5 mass% TiB_2 to 92 ± 36 nm at 1.0 mass%, 95 ± 37 nm at 1.5 mass%, and 97 ± 40 nm at 2.0 mass%. A stronger non-monotonic response was measured for agglomeration. The agglomerate fraction decreased from 12.6 ± 4.3% at 0.5 mass% to 7.3 ± 2.9% at 1.0 mass% and 6.1 ± 2.4% at 1.5 mass%, after which a slight increase to 6.7 ± 3.1% was measured at 2.0 mass%. Particle–matrix interfacial spacing decreased correspondingly from 18 ± 6 nm to 16 ± 5 nm and subsequently to approximately 15 ± 4–5 nm. The 1.0–1.5 mass% range was therefore associated with the most favorable combination of high particle density and limited agglomeration.

The through-height microstructural response of recycled AA7075 containing 1.0 mass% TiB_2 was resolved by EBSD, as shown in Figure 7b. An indexing rate of 95.2% was achieved using a 0.5 μm step size. Elongated grains were observed within approximately the first 0–12 mm above the substrate, where preferential alignment with the

build direction was evident. This morphology was associated with strong directional heat extraction through the substrate during the early deposition stages.

A transition toward finer and more equiaxed grains was observed at approximately 12–15 mm build height. Above this region, the middle and upper portions of the wall were dominated by spatially heterogeneous but substantially more equiaxed grains. The particle-assisted nucleation response was therefore sufficient to weaken the highly directional grain morphology that had been generated near the substrate. Repeated reheating during subsequent layer deposition did not re-establish the strongly elongated structure once a more equiaxed solidification mode had developed.

Quantitative grain-size distributions are presented in Figure 7c. Median grain sizes of 122 μm for primary AA7075 without TiB_2 and 95 μm for recycled AA7075 without TiB_2 were measured. Progressive grain refinement was then observed with particle addition, and median sizes of 61, 38, and 32 μm were obtained at 0.5, 1.0, and 2.0 mass% TiB_2, respectively. Corresponding interquartile ranges decreased from 78–181 μm to 60–144, 38–96, 24–62, and 20–51 μm across the investigated material conditions. Relative to primary AA7075 without TiB_2, a 73.8% reduction in median grain size was achieved at 2.0 mass% TiB_2.

Grain morphology changed concurrently. The median grain aspect ratio decreased from 6.8 for primary AA7075 to 4.7 for recycled AA7075 without TiB_2 and subsequently to 2.6, 1.8, and 1.6 as the TiB_2 addition increased. The equiaxed-grain fraction increased from 0.21 to 0.33 and then to 0.52 and 0.68 as the TiB_2 addition reached 1.0 and 1.5 mass%, respectively. At 2.0 mass%, the equiaxed fraction decreased slightly to 0.63. The decline at the highest particle content corresponded with the measured increase in agglomeration and decrease in effective particle number density. Consequently, the finest median grain size did not coincide with the highest measured equiaxed-grain fraction, and particle dispersion quality was shown to have influenced nucleation efficiency in addition to nominal TiB_2 concentration.

Crystallographic texture was weakened by both increasing build height and TiB_2 modification, as shown in Figure 7d. For recycled AA7075 without TiB_2, maximum texture intensity decreased from approximately 65–70 multiples of random distribution (m.r.d.) near the substrate to approximately 8–9 m.r.d. at a height of 40 mm. At 0.5 mass% TiB_2, a reduction from approximately 30 to 6 m.r.d. was measured. At 1.0 mass%, texture intensity decreased from approximately 13 to 2.5 m.r.d. Values below approximately 5 m.r.d. were measured throughout the build at 1.5 mass% TiB_2, while values of approximately 3 to 1.2 m.r.d. were obtained at 2.0 mass%.

Kernel average misorientation also decreased strongly with increasing TiB_2 concentration. Without TiB_2, values of approximately 0.8–2.6° were measured across the build-height range. At 2.0 mass% TiB_2, approximately 0.15–0.55° was measured. The reduction in local misorientation was consistent with the finer and less directionally constrained grain structure. Reduced texture intensity and lower local misorientation were therefore produced simultaneously as particle-assisted grain refinement became more effective.

Taken together, the particle and EBSD measurements demonstrated that TiB_2 concentration alone had not governed refinement efficiency. Particle number density, agglomeration, and spatial dispersion had acted together. The 1.0–1.5 mass% TiB_2 range produced the most favorable balance between particle availability, equiaxed-grain formation, texture weakening, and dispersion quality, whereas the highest nominal addition was accompanied by a small loss of effective particle dispersion.

Process–Structure–Property Relationships and Mechanical Response

The relationships among deposition conditions, thermal history, internal defects, microstructure, hardness, and mechanical response were evaluated by spatial and statistical correlation. The resulting correlation structure, hardness map, orientation-dependent tensile properties, and location-dependent fracture and fatigue responses were summarized in Figure 8.

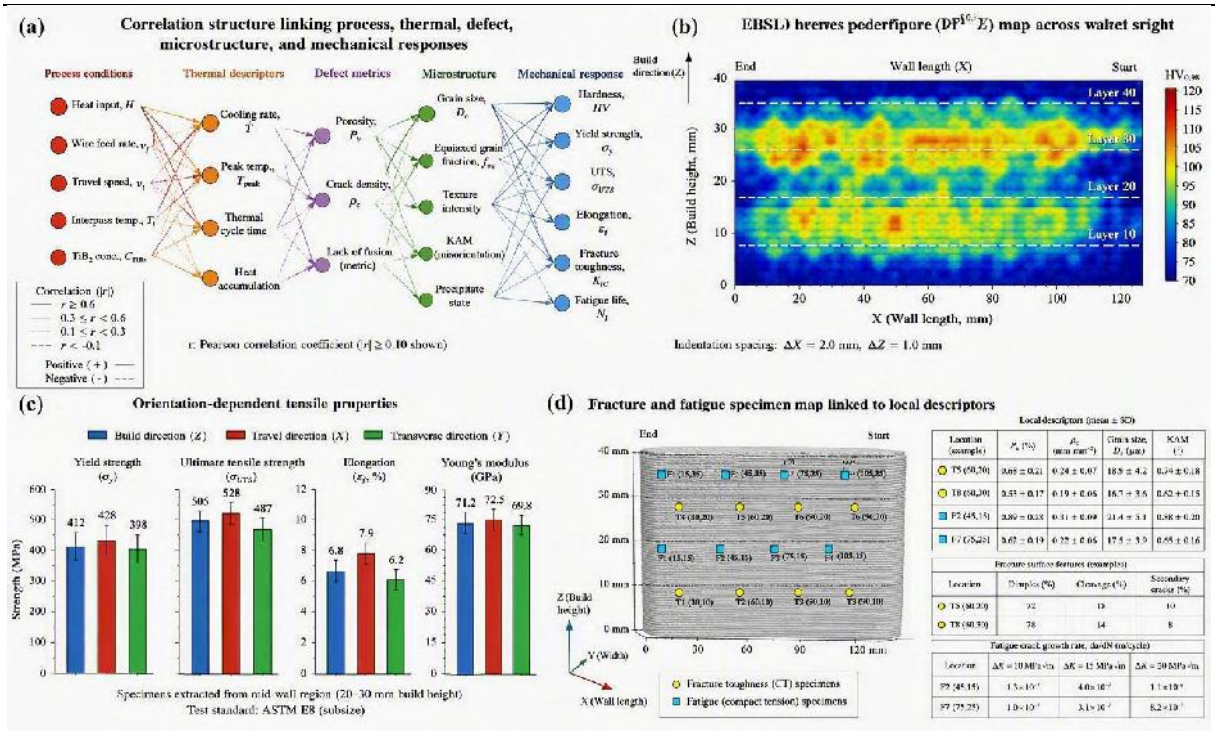

Figure 8. (a) Correlation structure linking deposition parameters, thermal descriptors, defect populations, microstructural variables, and mechanical properties; (b) spatial distribution of Vickers hardness over wall length and build height; (c) orientation-dependent yield strength, ultimate tensile strength, elongation, and Young's modulus; and (d) spatially registered fracture and fatigue specimen locations with local defect, microstructural, fracture-surface, and fatigue-crack-growth descriptors.

The correlation structure presented in Figure 8a demonstrated that the final mechanical response had been established through coupled process–thermal–defect–microstructure pathways rather than by direct dependence on any single deposition variable. Heat input, wire-feed rate, travel speed, interpass temperature, and TiB_2 concentration were associated with cooling rate, peak temperature, thermal-cycle duration, and cumulative thermal exposure. These thermal descriptors were subsequently associated with porosity, hot-crack density, and lack-of-fusion metrics. Grain size, equiaxed-grain fraction, texture intensity, kernel average misorientation, and precipitate condition were then related to hardness, yield strength, ultimate tensile strength, elongation, fracture toughness, and fatigue behavior.

The strongest correlations, defined by $|r| > 0.6$, were concentrated along the heat-input-to-thermal-history and microstructure-to-mechanical-property pathways. TiB_2 modification was therefore associated primarily with heterogeneous nucleation, grain morphology, and crack-path modification, whereas heat input was associated more strongly with thermal accumulation, defect formation, and precipitation-related changes. The correlation structure supported a sequential process–structure–property interpretation rather than a direct composition-to-strength relationship.

A spatially heterogeneous hardness distribution was measured across the deposited wall, as shown in Figure 8b. Values ranged from approximately 70 to 120 HV0.98. Hardness levels of approximately 70–85 HV0.98 were measured along portions of the lower and outer wall boundaries. Broad regions of approximately 95–110 HV0.98 were observed between build heights of approximately 8 and 32 mm. Local maxima approaching 115–120 HV0.98 were detected near $X = 50$–70 mm and $Z = 10$–15 mm, and a second region of elevated hardness was measured at approximately $Z = 25$–30 mm.

Lower hardness was measured toward the uppermost deposited region, where fewer reheating cycles had been experienced. The spatial response was associated with variations in precipitation state, solute redistribution, recovery, and defect content generated by the nonuniform thermal history. The middle wall region had undergone

repeated reheating and was therefore differentiated from both the substrate-influenced lower region and the more recently deposited upper layers.

Orientation-dependent tensile behavior was measured as shown in Figure 8c. Specimens loaded along the travel direction produced the highest measured yield strength, ultimate tensile strength, elongation, and Young's modulus, with respective values of 428 MPa, 528 MPa, 7.9%, and 72.5 GPa. Build-direction specimens produced values of 412 MPa, 505 MPa, 6.8%, and 71.2 GPa, respectively. Transverse specimens produced a yield strength of 398 MPa, an ultimate tensile strength of 487 MPa, an elongation of 6.2%, and a Young's modulus of 69.8 GPa.

Relative to the transverse orientation, travel-direction specimens exhibited increases of 30 MPa in yield strength, 41 MPa in ultimate tensile strength, 1.7 percentage points in elongation, and 2.7 GPa in elastic modulus. Directional anisotropy therefore remained measurable despite the substantial weakening of crystallographic texture produced by TiB_2 modification. The more favorable travel-direction response was associated with reduced loading across interlayer boundaries and with loading orientation relative to the residual texture and preferential crack directions.

Local fracture behavior was also related to the spatial defect and microstructural state, as summarized in Figure 8d. At specimen location T5, corresponding to approximately $X = 60$mm and $Z = 20$mm, porosity of 0.68 ± 0.21%, crack density of 0.24 ± 0.07 mm mm^{-2}, grain size of 18.9 ± 4.2 µm, and KAM of 0.74 ± 0.18° were measured. At T8, lower porosity and crack density values of 0.53 ± 0.17% and 0.19 ± 0.06 mm mm^{-2} were obtained, together with a smaller grain size of 16.7 ± 3.6 µm and a lower KAM of 0.62 ± 0.15°.

Corresponding changes were observed on the fracture surfaces. The dimple fraction increased from 72% at T5 to 78% at T8, while the cleavage fraction decreased from 18 to 14% and the secondary-crack fraction decreased from 10 to 8%. A more ductile fracture morphology was therefore associated with the location in which lower defect content, finer grains, and reduced local misorientation had been measured. This location-sensitive relationship agreed with the broader dependence of fracture response on locally registered structural descriptors rather than nominal build parameters alone (Lakshmaiya, 2026).

A comparable trend was measured during fatigue crack-growth testing. Higher crack-growth rates were measured at F2 than at F7. At stress-intensity ranges of 10, 15, and 20 MPa√m, crack-growth rates of 1.3×10^{-7}, 4.0×10^{-7}, and 1.1×10^{-6}m cycle^{-1} were measured at F2. Corresponding values of 1.0×10^{-7}, 3.1×10^{-7}, and 8.2×10^{-7}m cycle^{-1} were measured at F7. Reductions of approximately 23.1%, 22.5%, and 25.5% were therefore obtained at the respective stress-intensity ranges.

At F2, porosity, crack density, grain size, and KAM were measured as 0.89 ± 0.28%, 0.31 ± 0.09 mm mm^{-2}, 21.4 ± 5.1 µm, and 0.88 ± 0.20°, respectively. Lower corresponding values of 0.62 ± 0.19%, 0.22 ± 0.06 mm mm^{-2}, 17.5 ± 3.9 µm, and 0.65 ± 0.16° were measured at F7. Faster fatigue-crack propagation was therefore associated with the simultaneous presence of higher porosity, greater crack density, coarser grains, and increased local misorientation.

The mechanical results consequently reinforced the spatial analysis of the build. Tensile strength, fracture morphology, and fatigue-crack-growth response had not been determined solely by global process settings. Local thermal history, defect population, grain morphology, and crystallographic state had produced measurable differences within the same deposited structure.

Physics-Guided Defect Prediction and Predictive Uncertainty

The synchronized multimodal dataset was used to relate in situ process signatures to spatially registered porosity and hot-crack labels. The complete sensing and modeling framework, predictor importance, measured-versus-predicted defect fields, and probabilistic calibration results were summarized in Figure 9.

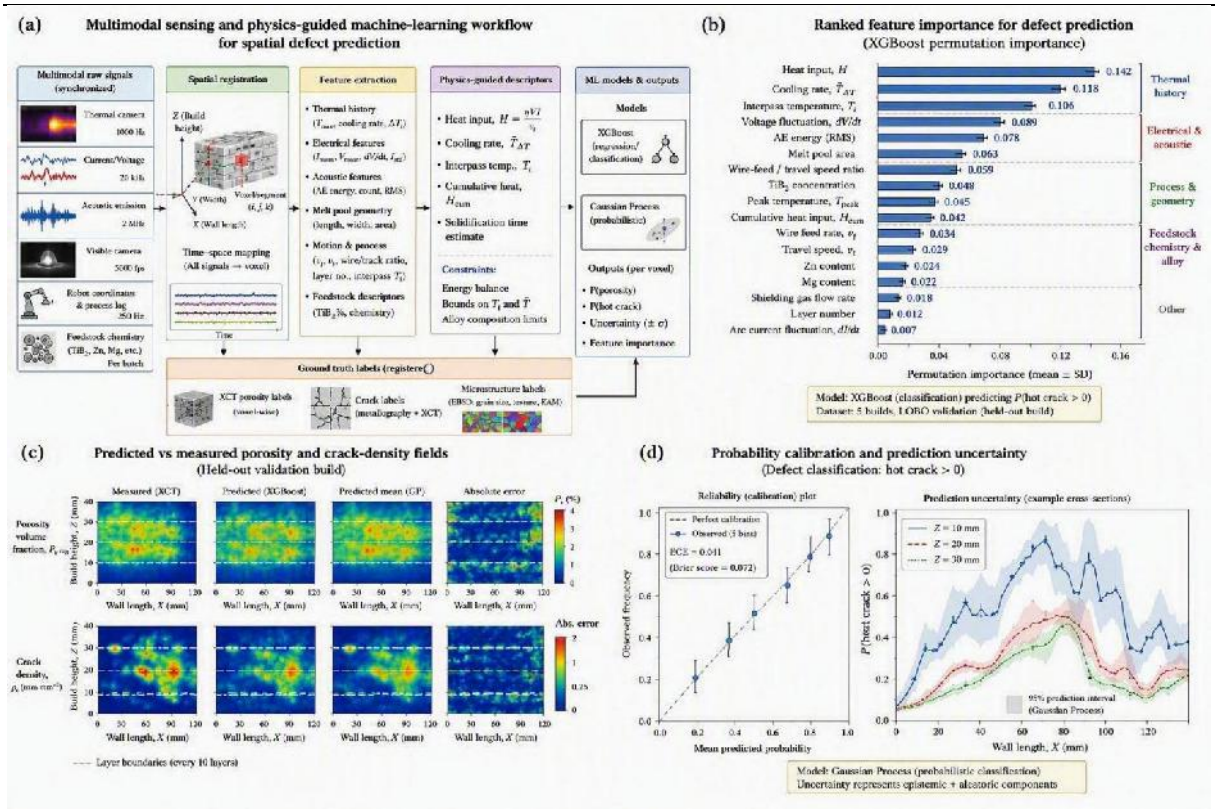

Figure 9. (a) Multimodal sensing, spatial registration, physics-guided feature extraction, model training, and ex situ ground-truth labeling workflow; (b) ranked permutation importance of thermal, electrical, acoustic, geometric, process, and compositional predictors; (c) measured and predicted porosity and crack-density distributions with corresponding absolute-error fields; and (d) probability calibration and Gaussian-process prediction uncertainty at selected build heights.

Thermographic data acquired at 1000 Hz, electrical signals acquired at 20 kHz, acoustic-emission data acquired at 2 MHz, visible images acquired at 5000 frames s^{-1}, robot coordinates recorded at 250 Hz, and feedstock chemistry measurements were synchronized and mapped into a common wall coordinate system, as summarized in Figure 9a. Thermal, electrical, acoustic, melt-pool, motion, process, and compositional features were then extracted. Heat input, cooling rate, interpass temperature, cumulative thermal exposure, and estimated solidification time were incorporated as physics-guided descriptors. Ground-truth labels were derived from XCT porosity, registered metallographic and XCT crack measurements, and EBSD-derived microstructural data. Deterministic predictions were generated using XGBoost, whereas probabilistic prediction and uncertainty estimation were performed using Gaussian-process models.

The permutation-importance ranking shown in Figure 9b demonstrated that thermal-history descriptors had contributed most strongly to hot-crack prediction. Heat input was ranked first with a permutation importance of 0.142 ± its model-derived variation. Cooling rate and interpass temperature followed with importance values of 0.118 and 0.106, respectively. Voltage fluctuation contributed 0.089, acoustic-emission root-mean-square amplitude contributed 0.078, and melt-pool area contributed 0.063.

The wire-feed-to-travel-speed ratio and TiB_2 concentration contributed 0.059 and 0.048, respectively. Peak temperature, cumulative heat input, wire-feed rate, and travel speed contributed 0.045, 0.042, 0.034, and 0.029. Zn and Mg concentrations contributed 0.024 and 0.022. Shielding-gas flow rate, layer number, and current fluctuation contributed 0.018, 0.012, and 0.007, respectively.

The ranking demonstrated that defect prediction had been dominated by descriptors associated with thermal history rather than by nominal machine settings alone. Nevertheless, measurable information had also been supplied by electrical, acoustic, melt-pool, particle-content, and chemical descriptors. The comparatively low

importance assigned to current fluctuation agreed with the stable electrical behavior that had been measured during the representative layer in Figure 5b. Process stability at the current-signal level therefore had not eliminated the importance of other transient sensing modalities.

Measured and predicted spatial defect fields for the held-out build were compared in Figure 9c. The central-upper porosity maximum and the broader middle-wall porosity band were reproduced by both the XGBoost and Gaussian-process models. Absolute porosity errors were generally below approximately 1%, although localized errors approaching 2–3% were measured near sharp defect boundaries and isolated peaks.

The principal crack-density regions near approximately $X = 60–95$ mm and $Z = 15–22$ mm were also reproduced. Prediction error was smaller in smoothly varying regions and increased where crack density changed abruptly over short spatial distances. The models therefore reproduced broad defect structures more effectively than narrow, high-gradient features. This behavior was consistent with spatial averaging introduced by the feature and learning framework, which had improved generalization across the wall while reducing sensitivity to highly localized defect transitions. Similar challenges associated with spatial process variability in CMT-based WAAM had been discussed by Shunmugesh et al. (2025).

Probability calibration was evaluated as shown in Figure 9d. The calibration curve followed the ideal diagonal closely, and an expected calibration error of 0.041 and Brier score of 0.072 were obtained. Predicted probabilities near approximately 0.2, 0.4, 0.5, 0.7, 0.8, and 0.9 corresponded closely with observed defect frequencies. Wider uncertainty intervals were measured at intermediate predicted probabilities, where greater ambiguity between defect and non-defect states had been present.

Cross-sectional probability distributions revealed the highest hot-crack probability at $Z = 10$mm. A maximum probability of approximately 0.85–0.90 was obtained near $X = 70–80$ mm. At $Z = 20$and 30 mm, maximum probabilities of approximately 0.50 and 0.45 were measured, respectively. The 95% prediction intervals widened around probability maxima and in wall-length regions where observations had been sparse or defect gradients had changed rapidly.

The probabilistic output therefore supplied information that was not available from deterministic point estimates alone. Regions associated with both high predicted crack probability and wide prediction intervals were distinguished from regions in which low probability had been predicted with greater confidence. Such spatial differentiation provided a basis through which high-risk locations could be prioritized for additional inspection or for subsequent process-control intervention.

Material Efficiency, Energy Demand, and Environmental Sensitivity

Material and environmental performance were evaluated for conventional primary-AA7075 manufacture, primary-wire WAAM, and the recycled-chip-to-wire WAAM route. The system boundaries, mass flow, cumulative energy-demand contributions, and sensitivity analysis were summarized in Figure 10.

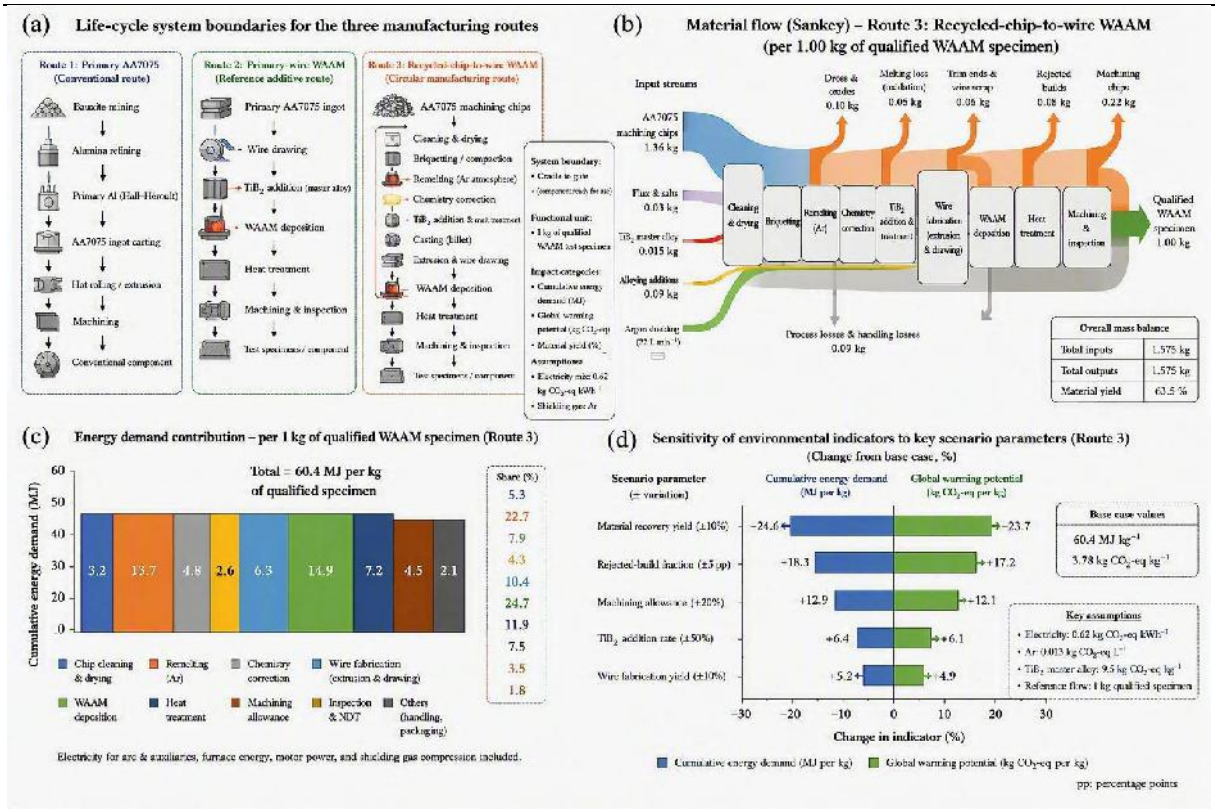

Figure 10. (a) Cradle-to-gate system boundaries applied to conventional primary-AA7075 manufacture, primary-wire WAAM, and recycled-chip-to-wire WAAM; (b) material flow of the recycled route normalized to 1 kg of qualified WAAM material; (c) process-stage contributions to cumulative energy demand; and (d) sensitivity of cumulative energy demand and global-warming potential to recovery yield, rejected-build fraction, machining allowance, TiB_2 addition, and wire-fabrication yield.

A cradle-to-gate boundary was applied to all three routes, as shown in Figure 10a. For the recycled route, chip cleaning, drying, briquetting, argon remelting, chemistry correction, TiB_2 incorporation, melt treatment, billet casting, extrusion, wire drawing, WAAM deposition, heat treatment, machining, and inspection were included. A functional unit of 1 kg of qualified WAAM material was used so that material yield, cumulative energy demand, and global-warming potential could be compared under a common basis.

The recycled-route mass balance is presented in Figure 10b. Inputs of 1.36 kg of AA7075 machining chips, 0.03 kg of flux and salts, 0.015 kg of TiB_2 master alloy, and 0.09 kg of alloying additions were recorded. Argon shielding was supplied at 22 L min^{-1} during deposition. Material losses included 0.10 kg of dross and oxides, 0.05 kg of melting loss, 0.06 kg of trim ends and wire scrap, 0.08 kg of rejected builds, 0.22 kg of machining chips, and 0.09 kg of other process and handling losses.

Total material inputs and outputs were balanced at 1.575 kg. A qualified product mass of 1.00 kg was obtained, corresponding to a material yield of 63.5%. Machining chips represented the largest recoverable output stream, whereas dross and oxidation represented the largest non-recoverable material loss.

The cumulative energy demand of the recycled route was calculated as 60.4 MJ kg^{-1} of qualified material, as shown in Figure 10c. WAAM deposition contributed 14.9 MJ, corresponding to 24.7% of the total. Argon remelting contributed 13.7 MJ, or 22.7%. Heat treatment contributed 7.2 MJ (11.9%), wire fabrication contributed 6.3 MJ (10.4%), chemistry correction contributed 4.8 MJ (7.9%), and machining allowance contributed 4.5 MJ (7.5%). Chip cleaning and drying contributed 3.2 MJ (5.3%), TiB_2-related processing contributed 2.6 MJ (4.3%), and inspection contributed 2.1 MJ (3.5%). The remaining 1.8% was associated with handling, packaging, and other supporting operations.

Remelting and WAAM deposition together accounted for 47.4% of the cumulative energy demand. Energy consumption had therefore been distributed across both feedstock conversion and additive deposition rather than being dominated by a single processing stage. Improvement of the recycling route consequently depended on both melt-processing efficiency and stable deposition with limited build rejection.

The base-case global-warming potential was calculated as 3.78 kg CO_2-equivalent kg^{-1}, while the corresponding cumulative energy demand remained 60.4 MJ kg^{-1}. Sensitivity results are shown in Figure 10d. Material recovery yield produced the largest response among the evaluated variables. Under the improved-yield scenario, a ±10% change in recovery yield produced changes of −24.6% in cumulative energy demand and −23.7% in global-warming potential.

A five-percentage-point change in rejected-build fraction produced changes of 18.3% in energy demand and 17.2% in global-warming potential. A ±20% change in machining allowance produced corresponding changes of 12.9 and 12.1%. By comparison, a ±50% change in TiB_2 addition produced changes of only 6.4% in energy demand and 6.1% in global-warming potential. A ±10% change in wire-fabrication yield produced changes of 5.2 and 4.9%, respectively.

Environmental performance was therefore influenced more strongly by qualified material recovery, build rejection, and machining allowance than by the TiB_2 addition itself. This result was consistent with the process and defect analyses. The intermediate TiB_2 range of 1.0–1.5 mass% had produced high particle number density, low agglomeration, substantial grain refinement, weakened crystallographic texture, and improved crack-related microstructural characteristics without the reduction in dispersion efficiency measured at 2.0 mass%.

The process, structural, predictive, and environmental responses were thus linked through material yield. Stable electrical operation and controlled thermal input were associated with lower risk of spatially concentrated porosity and cracking, while improved defect control reduced the likelihood of build rejection and excessive machining allowance. Because the environmental penalties associated with rejected material and additional machining were substantially larger than those associated with TiB_2 consumption, improvement of deposition stability and defect avoidance had affected both structural performance and resource efficiency.

The greatest combined benefit was associated with the controlled process region in which wire-feed rate, travel speed, and interpass temperature had been balanced with an intermediate TiB_2 concentration. Within that region, particle-assisted grain refinement, reduced texture intensity, improved defect distribution, and stable deposition had been achieved without the dispersion penalty measured at the highest TiB_2 addition. The synchronized sensing and probabilistic defect-prediction framework further allowed high-risk wall regions and bead-transition locations to be distinguished from lower-risk regions, thereby linking process monitoring directly with structural quality and material-efficiency outcomes.

CONFLICT OF INTEREST STATEMENT:

The author(s) declared no potential conflicts of interest.

FUNDING DECLARATION:

No external funding was received for this study.

DATA AVAILABILITY

The datasets generated and/or analyzed during the current study are available from the corresponding author upon reasonable requests.

References

Arana, M., Ukar, E., Rodriguez, I., Iturrioz, A., & Alvarez, P. (2021). Strategies to reduce porosity in Al-Mg WAAM parts and their impact on mechanical properties. Metals, 11(3), 524. doi:10.3390/met11030524.

Baier, D., Weckenmann, T., Wolf, F., Wimmer, A., & Zaeh, M. F. (2023). Underlying methodology for a thermal process monitoring system for wire and arc additive manufacturing. Journal of Manufacturing and Materials Processing, 7(1), 10. doi:10.3390/jmmp7010010.

Ding, D., He, F., Yuan, L., Pan, Z., Wang, L., & Ros, M. (2021). The first step towards intelligent wire arc additive manufacturing: An automatic bead modelling system using machine learning through industrial information integration. Journal of Industrial Information Integration, 23, 100218. doi:10.1016/j.jii.2021.100218.

Du, W., Sun, G., Li, Y., & Chen, C. (2023). Process optimization, microstructure and mechanical properties of wire arc additive manufacturing of aluminum alloy by using DP-GMAW based on response surface method. Materials, 16(16), 5716. doi:10.3390/ma16165716.

Du, Y., Mukherjee, T., & DebRoy, T. (2021). Physics-informed machine learning and mechanistic modeling of additive manufacturing to reduce defects. Applied Materials Today, 24, 101123. doi:10.1016/j.apmt.2021.101123.

El Mehtedi, M., Buonadonna, P., Carta, M., El Mohtadi, R., Mele, A., & Morea, D. (2023). Sustainability study of a new solid-state aluminum chips recycling process: A life cycle assessment approach. Sustainability, 15(14), 11434. doi:10.3390/su151411434.

Fagersand, H. M., Morin, D., Mathisen, K. M., He, J., & Zhang, Z. (2024). Transferability of temperature evolution of dissimilar wire-arc additively manufactured components by machine learning. Materials, 17(3), 742. doi:10.3390/ma17030742.

Farias, F. W. C., Payão Filho, J. C., & Moraes e Oliveira, V. H. P. (2021). Prediction of the interpass temperature of a wire arc additive manufactured wall: FEM simulations and artificial neural network. Additive Manufacturing, 48, 102387. doi:10.1016/j.addma.2021.102387.

Gao, C., Wolff, S., & Wang, S. (2021). Eco-friendly additive manufacturing of metals: Energy efficiency and life cycle analysis. Journal of Manufacturing Systems, 60, 459–472. doi:10.1016/j.jmsy.2021.06.011.

Geng, R., Du, J., Wei, Z., Xu, S., & Ma, N. (2021). Modelling and experimental observation of the deposition geometry and microstructure evolution of aluminum alloy fabricated by wire-arc additive manufacturing. Journal of Manufacturing Processes, 64, 369–378. doi:10.1016/j.jmapro.2021.01.037.

Gierth, M., Henckell, P., Ali, Y., Scholl, J., & Bergmann, J. P. (2020). Wire arc additive manufacturing (WAAM) of aluminum alloy AlMg5Mn with energy-reduced gas metal arc welding (GMAW). Materials, 13(12), 2671. doi:10.3390/ma13122671.

Guo, S., Agarwal, M., Cooper, C., Tian, Q., Gao, R. X., Guo, W. G., & Guo, Y. B. (2022). Machine learning for metal additive manufacturing: Towards a physics-informed data-driven paradigm. Journal of Manufacturing Systems, 62, 145–163. doi:10.1016/j.jmsy.2021.11.003.

Hamrani, A., Agarwal, A., Allouhi, A., & McDaniel, D. (2024). Applying machine learning to wire arc additive manufacturing: A systematic data-driven literature review. Journal of Intelligent Manufacturing, 35(6), 2407–2439. doi:10.1007/s10845-023-02171-8.

Hauser, T., Da Silva, A., Reisch, R. T., Volpp, J., Kamps, T., & Kaplan, A. F. H. (2020). Fluctuation effects in wire arc additive manufacturing of aluminium analysed by high-speed imaging. Journal of Manufacturing Processes, 56, 1088–1098. doi:10.1016/j.jmapro.2020.05.030.

Hauser, T., Reisch, R. T., Breese, P. P., Nalam, Y., Joshi, K. S., Bela, K., Kamps, T., Volpp, J., & Kaplan, A. F. H. (2021a). Oxidation in wire arc additive manufacturing of aluminium alloys. Additive Manufacturing, 41, 101958. doi:10.1016/j.addma.2021.101958.

Hauser, T., Reisch, R. T., Breese, P. P., Lutz, B. S., Pantano, M., Nalam, Y., Bela, K., Kamps, T., Volpp, J., & Kaplan, A. F. H. (2021b). Porosity in wire arc additive manufacturing of aluminium alloys. Additive Manufacturing, 41, 101993. doi:10.1016/j.addma.2021.101993.

Langelandsvik, G., Akselsen, O. M., Furu, T., & Roven, H. J. (2021). Review of aluminum alloy development for wire arc additive manufacturing. Materials, 14(18), 5370. doi:10.3390/ma14185370.

Li, T., Chen, J., Zeng, L., Tuo, Z., Ren, J., Zheng, Z., & Wu, H. (2025). Microstructure and mechanical properties of TiB_2/TiC particle modified Al-Mg-Si alloys fabricated by wire-arc additive manufacturing. Materials, 18(9), 1978. doi:10.3390/ma18091978.

Pan, Y., Yu, M., Xu, C., Zhang, J., & Geng, L. (2024). High-performance 2319 aluminum alloy via CMT-WAAM: Microstructure, porosity, and mechanical properties. Metals, 14(7), 797. doi:10.3390/met14070797.

Ruhaizat, N. E., Yusuf, N. K., Lajis, M. A., Al-Alimi, S., Shamsudin, S., Tukiat, I. S. T., & Zhou, W. (2022). Effect of direct recycling hot press forging parameters on mechanical properties and surface integrity of AA7075 aluminum alloys. Metals, 12(10), 1555. doi:10.3390/met12101555.

Sabbar, H. M., Leman, Z., Shamsudin, S., Tahir, S. M., Jaafar, C. N. A., Ariff, A. H. M., Zahari, N. I., & Rady, M. H. (2021). The effect of solid-state processes and heat treatment on the properties of AA7075 aluminum waste recycling nanocomposite. Materials, 14(21), 6667. doi:10.3390/ma14216667.

Sarıkaya, M., Başcıl Önler, D., Dağlı, S., Hartomacıoğlu, S., Günay, M., & Królczyk, G. M. (2024). A review on aluminum alloys produced by wire arc additive manufacturing (WAAM): Applications, benefits, challenges and future trends. Journal of Materials Research and Technology, 33, 5643–5670. doi:10.1016/j.jmrt.2024.10.212.

Shen, Z., Wu, Z., Wang, T., Jia, T., & Liu, C. (2023a). Research on technology of 7075 aluminum alloy processed by variable polarity TIG additive manufacturing utilizing nanoparticle-reinforced welding wire with TiB_2. Crystals, 13(3), 399. doi:10.3390/cryst13030399.

Shen, Z., Wu, Z., Wang, T., Jia, T., & Liu, C. (2023b). Effect of heat treatment processes on the microstructure and mechanical properties of high-strength aluminum alloy deposited layers processed by fused arc additive manufacturing. Materials, 16(20), 6801. doi:10.3390/ma16206801.

Sinha, A. K., Pramanik, S., & Yagati, K. P. (2022). Research progress in arc based additive manufacturing of aluminium alloys—A review. Measurement, 200, 111672. doi:10.1016/j.measurement.2022.111672.

Wagiman, A., Mustapa, M. S., Shamsudin, S., Lajis, M. A., Asmawi, R., Rady, M. H., & Yahya, M. S. (2020). Effect of thermally-treated chips on density of AlMgSi alloys recycled using solid-state technique. Processes, 8(11), 1406. doi:10.3390/pr8111406.

Xia, C., Pan, Z., Polden, J., Li, H., Xu, Y., & Chen, S. (2022). Modelling and prediction of surface roughness in wire arc additive manufacturing using machine learning. Journal of Intelligent Manufacturing, 33(5), 1467–1482. doi:10.1007/s10845-020-01725-4.

Xiao, X., Waddell, C., Hamilton, C., & Xiao, H. (2022). Quality prediction and control in wire arc additive manufacturing via novel machine learning framework. Micromachines, 13(1), 137. doi:10.3390/mi13010137.

Yang, Q., Xia, C., Wang, H., Zhou, M., Gao, S., Li, B., & Liu, S. (2022). Microstructure and mechanical properties of TiB_2/AlSi7Mg0.6 composites fabricated by wire and arc additive manufacturing based on cold metal transfer (WAAM-CMT). Materials, 15(7), 2440. doi:10.3390/ma15072440.

Zhang, H., Wu, Q., Tang, W., & Yang, J. (2024). Acoustic signal-based defect identification for directed energy deposition-arc using wavelet time–frequency diagrams. Sensors, 24(13), 4397. doi:10.3390/s24134397.